Nano Research

Open Access

Review Article

Advanced porous thermoelectric materials: Design, construction, and application

Ruoyan Li, Bangzhi Ge ✉, and Chongjian Zhou

State Key Laboratory of Solidification Processing and Key Laboratory of Radiation Detection Materials and Devices, Ministry of Industry and Information Technology, Northwestern Polytechnical University, Xi'an 710072, China

Cite this article: *Nano Research*, **2025**, *18*, 94907308. https://doi.org/10.26599/NR.2025.94907308

ABSTRACT: Thermoelectric (TE) technology, capable of converting heat directly into electricity, holds great promise for applications requiring efficient energy output, such as wearable devices and aerospace vehicles. However, the widespread use of traditional TE materials is limited by challenges such as high density, brittleness, and coupling of thermoelectric parameters. Porous TE materials offer a potential solution by enabling lightweight, enhancing mechanical flexibility, and reducing thermal conductivity by rational design and precise control of the pore structure. This review examined recent advances in the construction of optimized pore structures, including the size, distribution, and geometry. We summarized the state-of-the-art synthesis and classification for porous TE materials, highlighting methods for tuning pore configurations to enhance TE efficiency. Additionally, we also collected the cutting-edge device ensemble strategies and demonstrated their application such as aerospace, temperature management, and medical devices. Finally, we took an outlook on the rational and intelligent design of pore structures and their integration into systems for energy output. This review provides new understanding of mechanisms and designs for porous TEs, and also offers valuable guidance for the development of next-generation materials and their application in innovative self-powered systems.

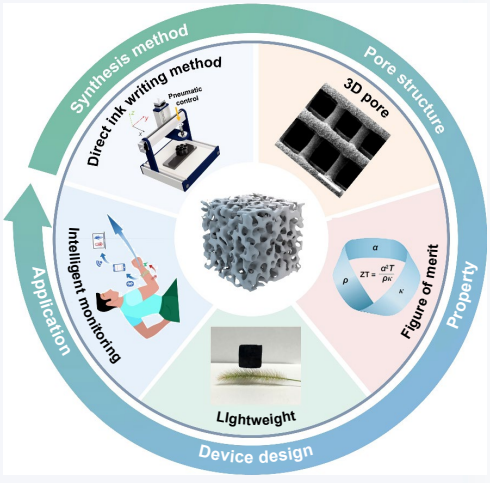

KEYWORDS: thermoelectric, pores, synthesis methods, mechanical properties, applications

1 Introduction

Thermoelectric (TE) materials, capable of directly converting heat into electricity, have become a central focus in the quest for efficient energy generation [1–3]. The performance of TE materials is measured by the dimensionless figure of merit (ZT), which is defined as

$$\mathrm{ZT} = S^2\sigma T/\kappa = S^2\sigma T/(\kappa_e + \kappa_L) \quad (1)$$

where S, σ, κ, T represents for the Seebeck coefficient, the electrical conductivity, the thermal conductivity, and absolute temperature, respectively [4–6]. The thermal conductivity κ is further decomposed into the contributions from carrier transport (κ_e) and lattice thermal conductivity (κ_L) [7, 8]. Accordingly, enhancing the TE performance primarily revolves around optimizing electrical properties and minimizing κ [9–13]. A higher ZT indicates superior TE efficiency, essential for practical applications. Widely used TE materials such as bismuth telluride (Bi_2Te_3) [14–16], lead telluride (PbTe) [17–19], and silicon-germanium (SiGe) [20–22] alloys have demonstrated success within specific temperature ranges. However, challenges, such as brittleness and heavy weight, have limited their broader applicability [23–27].

With the rise of advanced technologies, including wearable self-powered electronics [28, 29] and space exploration systems [30], the demands on TE materials have intensified. These cutting-edge applications require not only high efficiency but also lightweight, flexibility, and mechanical capacity [31–34]. For instance, wearable devices that harvest body heat require TE materials that are both highly efficient and adaptable to dynamic surfaces [35–37]. Likewise, the materials in radioisotope thermoelectric generator (TEG) (RTG) for aerospace craft is necessary to withstand extreme environments while maintaining high efficiency and durability [38–41]. More importantly, PbTe, the primary TE material for RTGs, offers a density 8 g·cm^{-3} with an order of magnitude heavier

Received: December 5, 2024; **Revised:** February 4, 2025
Accepted: February 14, 2025

✉Address correspondence to bangzhige@nwpu.edu.cn

than that of space vehicles 0.5 g·cm^{-3}. Consequently, development of lightweight, flexible and high-performance materials, is considered as a major challenge for TE technology.

One promising strategy to address these challenges is the incorporation of porous structures into TE materials [42–46]. Porosity not only decouples key TE parameters, such as σ and κ [47], but also enhances mechanical properties [48–50]. Through precise control of pore architecture, it is possible to design metamaterials with optimized thermal and electrical transport behaviors, while simultaneously improving flexibility and mechanical strength [51, 52]. Understanding how these porous structures influence the TE and mechanical properties is critical for the development of next-generation materials. Such advances will pave the way for innovative applications in energy harvesting, wearable technology, and other emerging fields, with the revolutionizing TE technology.

In this article, we present a comprehensive review of the recent advancements in porous TE materials, as shown in Fig. 1. Our focus starts with the synthesis methods for fabricating porous TE materials, including sintering process optimization, freeze-drying, direct ink writing, exclusion of porogenic agent, chemical etching, and other novel methods. We then categorize pores into four classes ranging from zero-dimensional (0D) to three-dimensional (3D) structures and expound on their distinctive characteristics. Subsequently, we discuss the impact of pore structures on thermal performance mechanisms and briefly outline recombination strategies, such as doping, defect incorporation, and the combination of nanostructures with porous designs, to effectively reduce the κ_L. More importantly, four design factors (high efficiency, flexibility, conformability, and lightweight) of TE devices are discussed in detail, and relevant examples are given to illustrate the role of porous structures in TE materials. Finally, we put forward several potential ideas and strategies to further enhance the performance of porous TE materials in the future.

2 Synthesis method for porous structure

2.1 Synthesis method

For TE, electricity is generated spontaneously by a given temperature difference driving charge carriers to transport from the hot to cold ends [64, 65]. In this process, the materials are desired to be thermally insulated while the electricity conducts along the heat flow direction, but this is difficult to achieve because of the coupling of the TE parameters [66, 67]. Rational design of microstructures can be more beneficial for the directional decoupling of TE parameters. Note that the pore in a material tends to scatter both phonons and charge carriers in the conventional perception. Accordingly, the introduction of tunable pore structures within the material by appropriate methodology is favorable for the decoupling of TE parameters. We summarize some representative methods to introduce pores in TE, including the sintering process optimization, freeze-drying method, direct ink writing, exclusion of porogenic agent, chemical etching method, and other novel

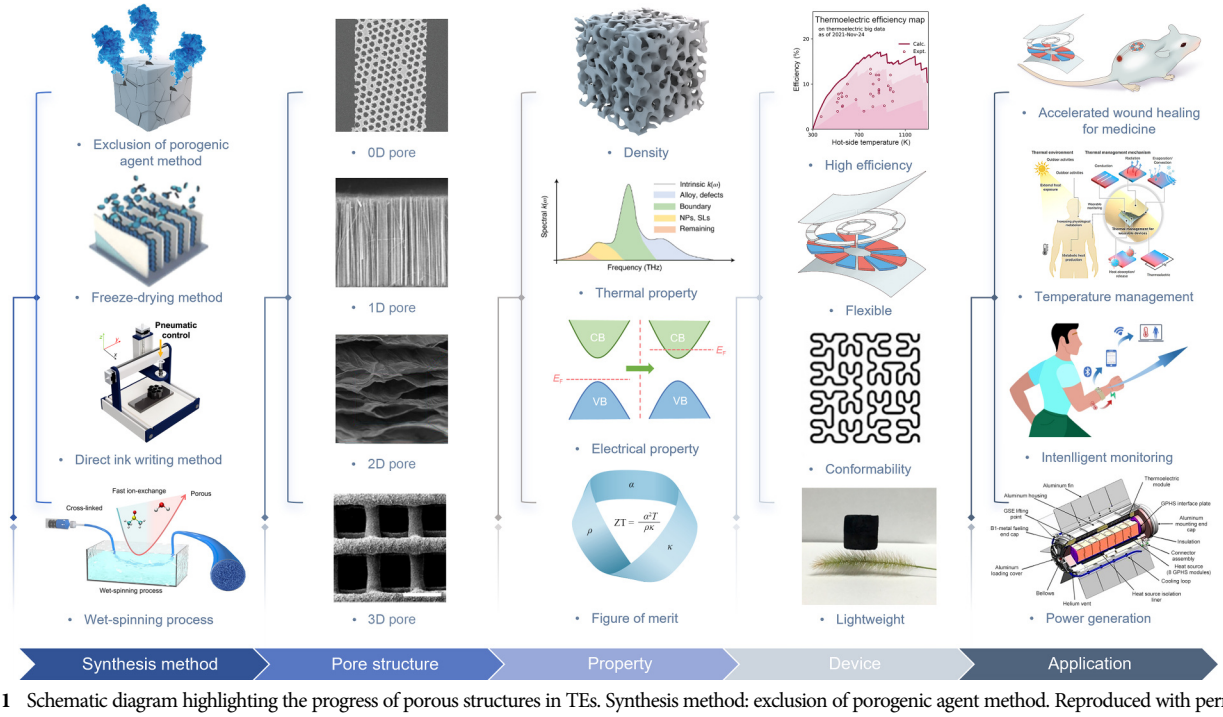

Figure 1 Schematic diagram highlighting the progress of porous structures in TEs. Synthesis method: exclusion of porogenic agent method. Reproduced with permission from Ref. [47], © Wiley-VCH GmbH 2021. Freeze-drying method. Reproduced with permission from Ref. [53], © WILEY-VCH Verlag GmbH & Co. KGaA, Weinheim 2019. Direct ink writing method. Reproduced with permission from Ref. [51], © Choo, S. et al. 2021. Wet-spinning process. Reproduced with permission from Ref. [48], © American Chemical Society 2023. Pore structure: 0D pore. Reproduced with permission from Ref. [54], © American Chemical Society 2010. 1D pore. Reproduced with permission from Ref. [55], © Elsevier Ltd. 2015. 2D pore. Reproduced with permission from Ref. [52], © Elsevier Ltd. 2016. 3D pore. Reproduced with permission from Ref. [49], © Kim, F. et al. 2021. Property: Thermal property. Reproduced with permission from Ref. [56], © Springer Nature Limited 2021. Figure of merit. Reproduced with permission from Ref. [57], © He, J. et al. 2017. Device: high efficiency. Reproduced with permission from Ref. [58], © Ryu, B. et al. 2023. Flexible. Reproduced with permission from Ref. [59], © Wiley-VCH GmbH 2024. Conformability. Reproduced with permission from Ref. [60], © Springer Nature Limited 2014. Lightweight. Reproduced with permission from Ref. [78], © American Chemical Society 2017. Application: accelerated wound healing for medicine. Reproduced with permission from Ref. [59], © Wiley-VCH GmbH 2024. Temperature management. Reproduced with permission from Ref. [61], © Yun, J. et al. 2023. Intelligent monitoring. Reproduced with permission from Ref. [62], © Yang, S. et al. 2023. Power generation. Reproduced with permission from Ref. [63], © Zoui, M. A. et al. 2020.

methods.

2.1.1 *Sintering process optimization*

For most TE bulk, spark plasma sintering (SPS) or hot-press sintering technologies are the most commonly applied methods for densifying the powder. During the densification process, atoms on the surface of the particles diffuse into each other to form grain boundaries connecting the grains together due to the applied temperature and pressure. Namely, the pores between the incompact particles will be closed and thus densified. A reasonable regulation in sintering pressure, temperature, even the size or morphology of the raw powder can contribute to the formation of pores by retaining spaces among the particles [68]. For example, Zhang et al. synthesized the mesoporous Bi_2Te_3 particles with the uniform and controllable pore size using chemical method [69]. In the following, the raw particles were densified using the hot-pressed equipment into a mechanically stable porous bulk. Importantly, most of the porosity in the bulk results from the synthetic mesopores that are created by raw powder. For the effect of sintering pressure in porous TE materials, a case is displayed by Wu et al.'s work [70]. The Sb doped $Mg_2Si_{0.5}Sn_{0.5}$ sample with a porosity of 37% was sintered without sintering pressure during the SPS, while the sintered sample was dense at 50 MPa of sintering pressure. The fabrication of porous oxide TE ceramics is also a good example for temperature regulation. Because of high melting point, the grain boundaries of oxide ceramics are gently bonded during sintering. Size-controlled pores can be easily obtained by tuning the sintering temperature. The porous Ga-doped In_2O_3 TE ceramics with 67.2% of porosity were synthesized via a hydrothermal method combined with SPS at 723 K. Their porosity decreases to 10.1% with higher sintering temperature to 1273 K [71]. In contrast, a higher sintering temperature may generate more pores in the Ag_2X-based (X = S, Se, and Te) system synthesized using solution methods. As the sintering temperature increases from 373 to 773 K, the porosity of β-Ag_2Se increases from 6.6% to 11.7%, which may be attributed to the fast fusing process of nanosized Ag_2Se powders with high surface energy [72]. Note that insufficient sintering may affect the bond strength of the grains. Excessive reduction of temperature and pressure in sintering process can lead to a deterioration of the quality of the grain boundaries and thus damage the carrier mobility. The porous β-Ag_2Se work shows a good example of obtaining higher porosity at high temperatures, boosting charge mobility while reducing κ.

2.1.2 *Freeze-drying method*

Freeze-drying method is also called ice template method. In this process, the mixed solution of solvent and TE particles is frozen in an ice bath. As low temperatures cause the liquid to freeze as a template, TE particles are therefore assembled with ice as a template. Afterwards, the resulting frozen mixture was freeze-dried at low temperatures until all the ice was sublimated, leaving a porous structure of TE particles seen in Fig. 2(a). The structure for pore size, volume, and morphology can be manipulated by parameters such as freeze temperature, solution concentration, nature of solvent and solute, and temperature gradient [73–75]. For example, Guo et al. fabricated porous graphene films (PGFs) through this method. First, the graphite oxide is submerged in water forming a polymeric hydrogel network that is ionically crosslinked. This is followed by quick-freezing in liquid nitrogen, in which the remaining moisture is quickly frozen. The water is sublimated in the further freeze-drying process, leaving a microporous network structure in the material [52, 76]. With a similar preparation strategy, porous composites can also be prepared such as poly(3,4-ethylenedioxytiophene)-tosylate (PEDOT-Tos)/single-walled carbon nanotube (SWCNT) TE aerogels and reduced graphene oxide (rGO)/SWCNT hybrid aerogels [77, 78]. It is important to note here that the TE aerogels prepared by freeze-drying can be manipulated to introduce a substantial number of pores with controllable size and distribution. Even the resulting materials can be flexible and bendable. However, excessive porosity

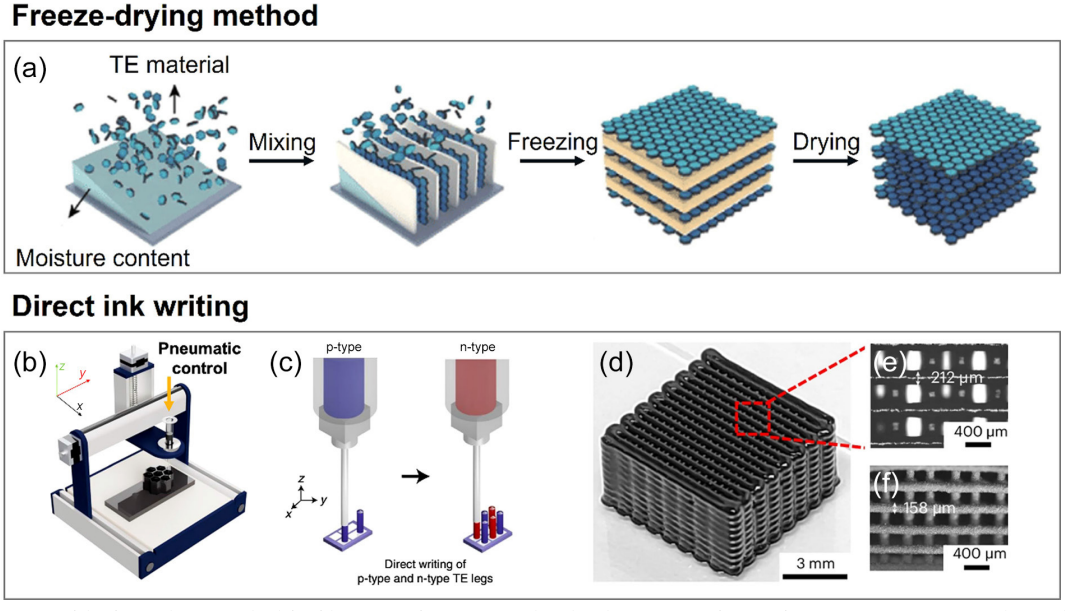

Figure 2 (a) Schematic of the freeze-drying method for fabrication of pores. Reproduced with permission from Ref. [53], © WILEY-VCH Verlag GmbH & Co. KGaA, Weinheim 2019. Schematic for direct ink writing method: (b) scheme for 3D printing process of the Cu_2Se-based honeycomb cellular architecture by using allinorganic $Cu_{2-x}Se$ ink. Reproduced with permission from Ref. [51], © Choo, S. et al. 2021. (c) Schematic showing the fabrication of the microTEG (μTEG) by direct 3D ink writing. Reproduced with permission from Ref. [49], © Kim, F. et al. 2021. ((d) and (e)) A photograph (d) and OM image (e) of the as-printed 3D lattice structure constructed of layer-by-layer-deposited Cu_2Se ink filaments. (f) OM images of the sintered 3D Cu_2Se lattice. Reproduced with permission from Ref. [81], © Choo, S. et al. 2024.

and weak interfacial bonding result in the TE properties of aerogels hardly reaching the level of bulks.

2.1.3 *Direct ink writing method*

The one of challenges is to fabricate TE devices with an appropriate size and shape for microstructure to match the distribution of the heat field. The homogeneous bulks prepared by SPS or hot pressing are difficult to match exactly with the heat field. The methods of direct ink writing, 3D printing technologies, have introduced a revolution in manufacturing, allowing the fabrication of complex and controllable 3D shapes from a variety of materials (Figs. 2(b) and 2(c)) [79, 80]. For example, to design the topology of Cu_2Se TE legs for higher power generating efficiency and mechanical durability, Choo et al. designed the Cu_2Se TE legs with honeycomb-like pores using 3D finite element models for higher power generating performances and stronger mechanical stiffness than a typical cuboid. The designed objective model was achieved by the direct ink writing method [51]. Very recently, this group increased the concentration of solutes in the glycerol solvent medium, improving the 3D printability of the ink [81]. This also enables the construction of more complex structures, including hourglass, arch, and lattice structures constructed from directly written filaments. Figures 2(d)–2(f) show the photograph and optical microscopy (OM) images of printed filaments, indicating their smooth surface and uniform thickness. Zhang et al. developed porous 3D TEs which can be used for on-site energy harvesting [82]. Complex 3D-printed $Bi_{0.5}Sb_{1.5}Te_3$ (BST) open cellular-like structures with high specific surface area were fabricated for a high rate of heat transfer throughout the heat pipes [83]. Note that the printability of TE inks is a serious challenge for printing high-precision configurations. For the resolution of this issue, Kim et al. were devoted to printability of direct writing of particle-based TE inks to prepare the microscale 3D TE architectures [49]. By manipulating various characteristics of TE particles (including size distribution and surface charge states), TE inks were created with high viscoelasticity. Then, the inks for direct 3D writing were employed to print filaments in a one-dimensional (1D)-controlled manner at the high precision level within 180 μm, constituting the high-performance 3D TE architectures including pores and lattices. The resulting structures exhibit high TE figures of merit even comparable to those of bulk. Very importantly, the authors directly printed miniature π-type TE devices including p- and n-type legs exhibiting large temperature gradients and a power density of 480 $\mu W \cdot cm^{-2}$.

2.1.4 *Exclusion of porogenic agent method*

The porogenic agent is removed during high-temperature sintering or annealing, leaving pores in the matrix, as shown in Fig. 3(a). Because of the sufficient sintering temperature and pressure, the materials obtained by the method of exclusion of porogenic agent method possess strong grain boundary bonding, but also generate pores with controlled concentration and morphology by manipulating the amount and the shape of the porogenic agent [84–88]. Hu et al. synthesized a porous tetrahedrite $Cu_{12}Sb_4S_{13}$ network by the sublimation of porogenic agent BiI_3 during annealing and modulated microstructure simultaneously. The network-like porous structure of $Cu_{12}Sb_4S_{13}$ is formed by sublimation of BiI_3 (595 K) and escaping through low-energy grain boundaries during annealing of the sample [47]. Very importantly, the introduction of pores in $Cu_{12}Sb_4S_{13}$ by volatilization of BiI_3 without significantly disrupting the charge mobility is significant for the decoupling of the TE parameters. Similarly, Atta U. Khan et al. found that small pores were paved in the $CoSb_3$ alloyed with Si and Te due to the evaporation of the Sb_2Te phase mainly at grain boundaries during high-temperature (higher than the melting point of this phase) annealing [89]. The hollow poly-silicon (pSi) TE nanotubes were obtained by chemical vapor deposition (CVD) combined with removal of porogenic agent. The fabrication method consists in electrospinned carbon-based fabrics as a sacrificial support for the deposition of thin silicon layers by CVD. The resulting thin silicon@C fabrics form nanotubes after removal

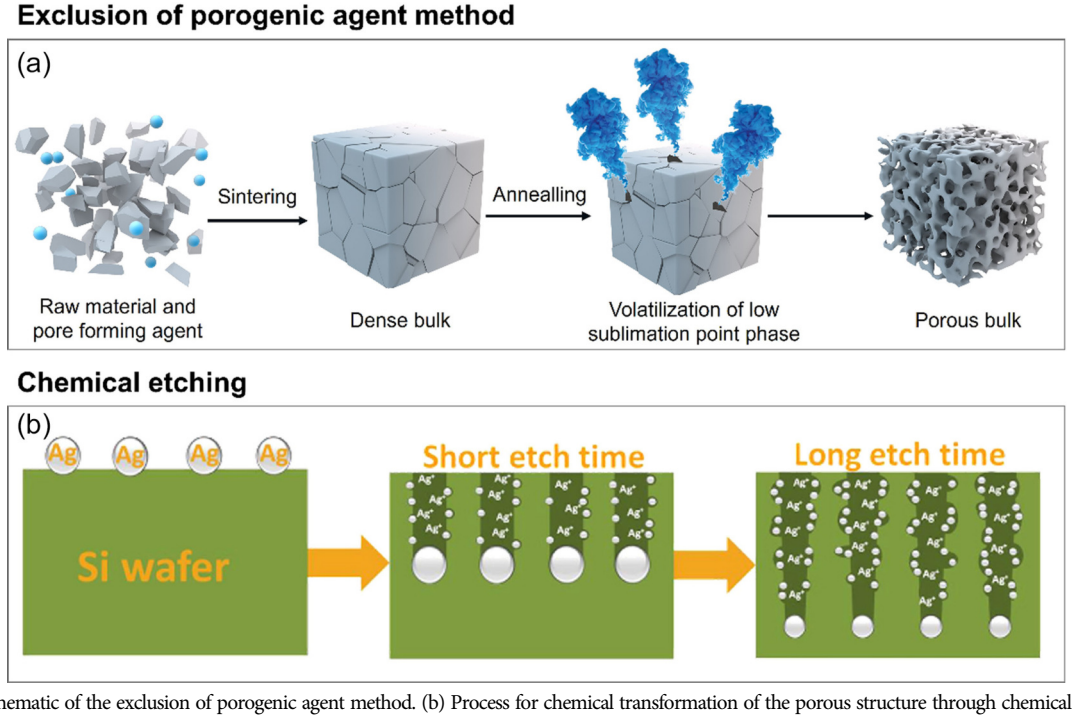

Figure 3 (a) Schematic of the exclusion of porogenic agent method. (b) Process for chemical transformation of the porous structure through chemical etching method. Reproduced with permission from Ref. [55], © Elsevier Ltd. 2015.

of the carbon template annealing at 1023 K in reducing atmosphere [90]. Importantly, the strategy for exclusion of porogenic agent helps to provide sufficient sintering temperatures and pressures to increase the bonding strength of the particles while creating pores. Moreover, controllability of the pores can be realized by controlling the shape and size of the porogenic agent. Consequently, this strategy provides a better decoupling of the TE parameters and obtains a higher performance.

2.1.5 *Chemical etching method*

The dense solid or particle is chemically etched to produce a large number of pores when it undergoes ion exchange with the more reactive reactants. Figure 3(b) shows a schematic of the chemical etching method. For example, Ag nanoparticles etch dense silicon wafers, thereby eroding a large number of vertical pores inside them and generating numerous silicon nanowires along the direction of the pores [91]. The technique is based on the electrochemical displacement of silicon by the reduction of $Ag^+ \rightarrow Ag^0$ on the wafer surface. The reaction takes place in an aqueous solution of $AgNO_3$ and HF acid. Namely, Ag^+ is reduced to the surface of the silicon wafer by giving holes for the valence band of silicon and oxidizing the surrounding lattice, which is then etched with HF. The Ag nanoparticles are formed from initial reduction of Ag^+ on the surface of the wafer, thus preventing the spatial extent of the processes for oxidation and etching processes. Following completion of the synthesis, the residual Ag on the array can be washed off with deionized water. The resulting pores and the remaining Si constitute a porous structure. Similarly, Boor et al. fabricated porous silicon samples using an electrochemical method by etching n-type silicon wafers in an aqueous solution containing 4.8% HF and 0.1 wt.% ionic surfactant [92].

Furthermore, Ju et al. have successfully prepared porous SnTe nanosheets (NSs) via an anion-exchange reaction of it in an organic acid solution [93]. In the presence of organic acids, Se^{2-} ions in SnSe are exchanged with Te^{2-} through hydrothermal reactions, resulting in the synthesis of SnTe NSs. In this process, the formation of the porous network-structure is transformed by the depletion and recrystallization of the flat NS structure of SnSe. In another work, the similar method was used to prepare the porous $SnSe_{0.8}S_{0.2}$ NSs [94]. The chemical etching method can introduce sufficiently abundant pores while ensuring a strong enough bond to the matrix. However, finding a suitable chemical etchant to accomplish particle exchange is the key to this technique.

2.1.6 *Other novel methods*

Besides the common methods described above, some special strategies have been used to successfully introduce porous structures for specific material systems. For instance, Zhao et al. displayed a paradigm for an ultrafast solid-state explosive reaction to fabricate nanoporous TE bulk including well-controlled sizes and distributions pore [95]. Note that compound Cu_2Se is formed by directly reacting Cu and Se when the energy of Cu_2Se is lower than Cu + Se with a release energy (ΔH) thermodynamically. The explosive reaction of Cu and Se powders was activated using SPS approach under tunable pressure. By using various sizes of raw particles, grain and pore sizes can be easily achieved in the porous bulk Cu_2Se. The other novel method is melt-centrifugation technique to introduce the large porosity and microscale dislocations (DS) in $(Bi, Sb)_2Te_3$ bulk (Fig. 4(a)). Pan et al. employed the melt-centrifugation to construct the microstructure by separating the liquid of molten eutectic phase mixture from the solid $(Bi, Sb)_2Te_3$ particles under high centrifugal force [96]. As a result, a large number of porous structures remain in $(Bi, Sb)_2Te_3$ bulk that are excluded from the melted liquid phase. As a result, lots of porous structures remain in $(Bi, Sb)_2Te_3$ bulk that are excluded from the melted liquid phase. Very recently, Li et al. reported stretchable n-type TE fibers based on the hybrid of $Ti_3C_2T_x$ MXene nanoflakes and polyurethane (PU) (MP) through a wet-spinning process for creating a 3D interconnected porous structure [48]. First, a spinning solution was mixt through the amalgamation of PU chains and dimethyl sulfoxide (DMSO) solvent with conductive two-dimensional (2D) $Ti_3C_2T_x$ MXenes. Subsequently, the resulting DMSO solvent was eliminated to induce the formation of stable fibers by carefully extracting the colloidal silk at a consistent rate within a water bath, leveraging its selective oil absorption and oil/water separation attributes (Fig. 4(b)). A homogeneous porous network of $Ti_3C_2T_x$ MXene-PU monomers with 3D interconnectivity was established through above rapid ion exchange at the interface (IF) of the fibers, resulting in outstanding mechanical robustness and stretchability of the material. Notably, the material exhibits an impressive fracture stress of up to 37 MPa.

Interestingly, Dun et al. successfully generated single nanoholes with the range of 5–100 nm in Bi_2Te_3 nanoplates through a solution-based approach in the schematic fabrication process shown in Fig. 4(c) [97]. The starting perfect hexagonal Bi_2Te_3 nanoplates with planes parallel to the basal plane were prepared as the base [98]. Subsequently, the intact nanoplates were subjected to postprocessing at different heating temperatures from 25 to 150 °C, leading to the redissolved Bi/Te atoms in the solvent of ethylene glycol and leaving a Kirkendall nanopores. The yield of Bi_2Te_3 nanoplates with a single nanohole exceeded 95%.

2.2 Pore structure

After introducing the methods for pore introduction, we will summarize the pore structure in the following section. Rational design of the pore structure can enhance physical properties of the material such as mechanical strength, κ suppression, flexibility, and density. In this section, the pore structure has been systematically summarized in terms of pore dimensions (0D, 1D, 2D, and 3D) and configurations (disordered, quasi-ordered, and ordered), aiming to provide a more profound understanding for how pore structure affects TE properties.

2.2.1 *0D pore*

The 0D pores are defined as pore sizes in the range of 0–100 nm in all three dimensions. Such pores are often employed as a scattering of phonons within the material to reduce κ_L, being the most commonly introduced pores in TE materials. For example, Jin et al. introduce the 0D disordered nano pores (Fig. 5(a)) in Cl-doped Bi_2S_3 systems using the method of sintering process optimization [68]. These disordered pores exhibit small sizes, high concentration, and a wide distribution range, which leads to strong phonon scattering, resulting in a minimum κ_L of 0.36 $W \cdot m^{-1} \cdot K^{-1}$ at 823 K, approximately 35% lower than that of the dense sample. However, this also inevitably leads to a significant degradation in the electrical properties, with the charge carrier mobility decreasing from 38 $cm^2 \cdot V^{-1} \cdot s^{-1}$ in the pure sample to 2.01 $cm^2 \cdot V^{-1} \cdot s^{-1}$. As a result, additional Cl doping was required in this work to compensate for the deterioration in the electrical transport properties.

Furthermore, Xu et al. purposefully designed the pore structure in PbS systems with a more regular distribution [98]. They

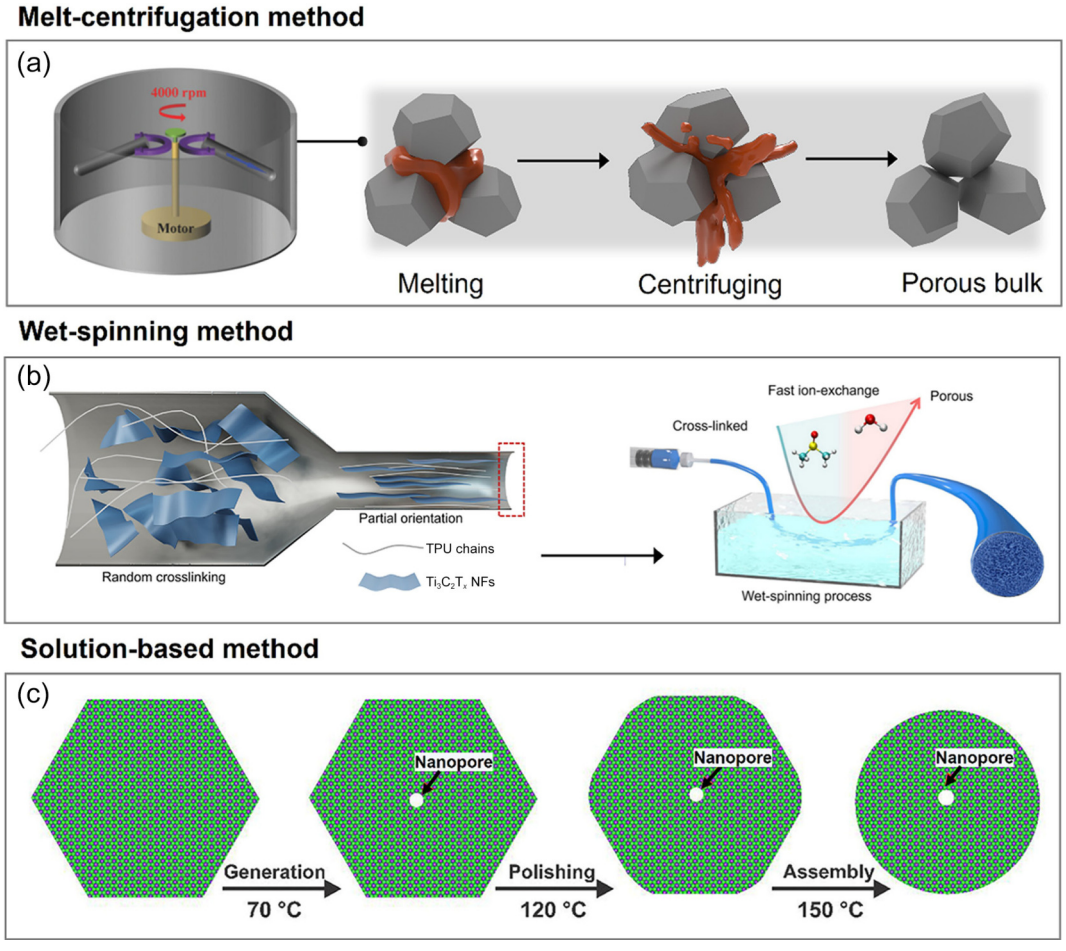

Figure 4 (a) Schematic illustration of melt-centrifugation method for porous (Bi, Sb)$_2$Te$_3$. Reproduced with permission from Ref. [96], © WILEY-VCH Verlag GmbH & Co. KGaA, Weinheim 2018. (b) The wet-spinning method for $Ti_3C_2T_x$ based using a 3D porous fiber. Reproduced with permission from Ref. [48], © American Chemical Society 2023. (c) The wet-chemical approach for Bi_2Te_3 nanoplates with individual nanopore. Reproduced with permission from Ref. [97], © American Chemical Society 2018.

synthesized convexity-controlled and tunable spatial packing PbS nanoparticles by employing solution-synthesized method. The bulk samples sintered from these nanoparticles showed a porosity of 18% and the pores are distributed along the grain boundaries with quasi-ordered manner (Fig. 5(b)). This deliberate refinement and design of the structure enhance the orderliness of the pore distribution within the material, resulting in a concomitant enhancement in σ, a diminishment in κ, and a notable elevation in ZT for PbS. Remarkably, a peak ZT value of 1.06 is attained at a temperature of 838 K.

Besides, to achieve a more ordered pore structure, Tang et al. employed a chemical etching method to fabricate high-density 0D nano-pores on single-crystal silicon membranes [54]. Figure 5(c) shows the scanning electron microscopy (SEM) image of the porous silicon ribbon produced through this method, with a pore interval of 350 nm. It can be observed that these pores are uniformly and orderly arranged on the silicon ribbon. By further reducing the pore spacing to 55 nm (with a porosity of 35%), the κ of the high-density silicon decreases by two orders of magnitude. The κ reduces from 50.9 W·m^{-1}·K^{-1} for the intrinsic sample to 2.03 W·m^{-1}·K^{-1}, approaching the amorphous limit. Additionally, due to the electron mean free path (MFP) in heavily doped silicon being in the range of 1–10 nm, shorter than the 55 nm pore spacing, no necking effect in electrical properties can be observed. Therefore, the ZT value reaches 0.4 at room temperature, which is 50 times enhancement in comparison to the non-porous silicon of the same thickness.

2.2.2 *1D pore*

The 1D pore is defined as its morphology being linear or distributed along a linear pathway. Xu et al. conducted an intriguing work to fabricate 1D porous n-type $Bi_2Te_{2.5}Se_{0.5}$ through sintering hollow nanorods by SPS [99]. Figure 5(d) shows a SEM image for the specimen machined using the focused-ion-beam (FIB), revealing that the initial $Bi_2Te_{2.5}Se_{0.5}$ nanoshell is crushed and reconsolidated into a porous structure among larger grains with disorderliness. Benefiting from a wide range of phonon frequency scattering and a large porosity, the κ_L decreases to a minimum value of 0.14 W·m^{-1}·K^{-1} at 463 K. However, compared to previous works, the carrier mobility of this material is significantly reduced, indicating that the disordered pore structure has a detrimental effect on the electrical properties [100–102].

Moreover, an quasi-ordered 1D pore structure was achieved in the work of Alex Morata et al. [90]. By the exclusion of porogenic agent method, the porous pSi nanotube fabric was obtained. After the carbon-based fabrics used as a sacrificial support are removed, a hollow silicon nanotube is left with a channel of the scale 5 μm (Fig. 5(e)). This quasi-ordered pore structure reduces the κ of the

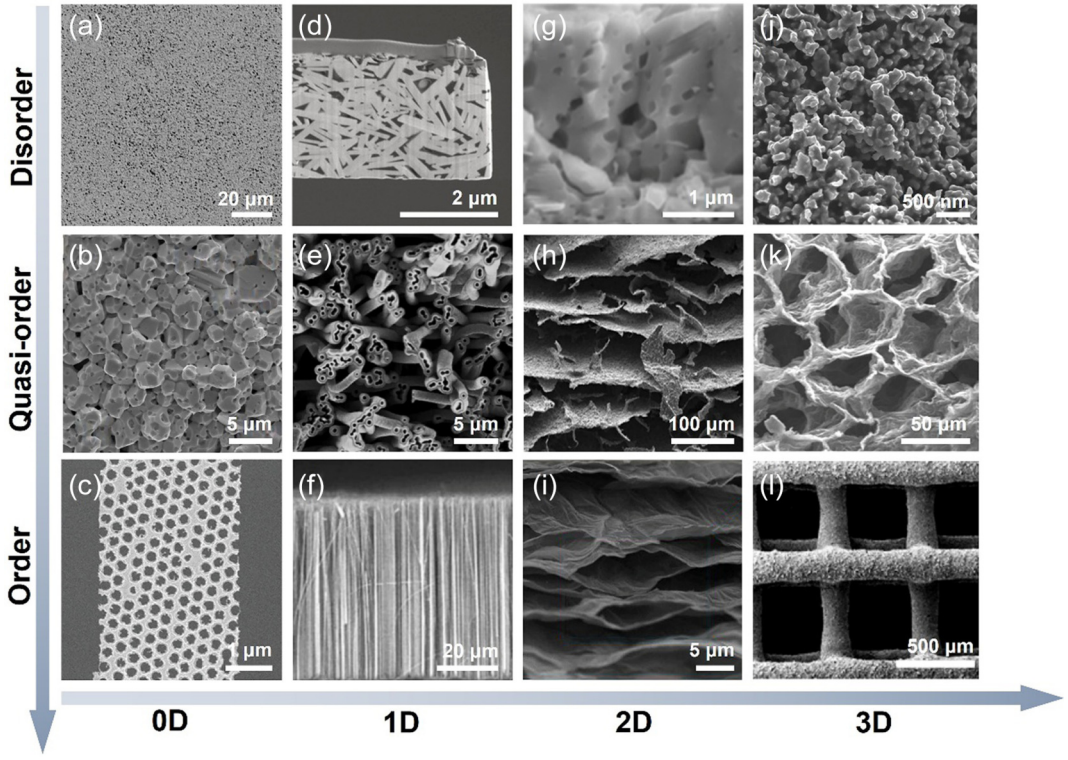

Figure 5 Morphologies of the pore structure from disorder to order (top to bottom) and across 0D to 3D architectures (left to right). (a) The Cl-doped Bi_2S_3 with 0D disordered nano pores introduced by the method of sintering process optimization. Reproduced with permission from Ref. [68], © Elsevier Ltd. 2022. (b) The quasi-ordered pores in sintered PbS by the solution-synthesized nanoparticles. Reproduced with permission from Ref. [98], © American Chemical Society 2018. (c) The 0D nano-pores in single-crystal silicon membranes produced with chemical etching method. Reproduced with permission from Ref. [54], © American Chemical Society 2010. (d) The FIB-cut $Bi_2Te_{2.5}Se_{0.5}$ sample with 1D pores sintered using hollow nanoshell. Reproduced with permission from Ref. [99], © Wiley-VCH Verlag GmbH & Co. KGaA, Weinheim 2017. (e) The cross-sectional images of the poly-silicon nanotube fabrics with quasi-ordered 1D pores obtained by the exclusion of porogenic agent method. Reproduced with permission from Ref. [90], © Morata, A. et al. 2018. (f) Cross-section of the chemically etched 1D ordered pores in silicon nanowire arrays. Reproduced with permission from Ref. [55], © Elsevier Ltd. 2015. (g) Cross-sectional SEM image for 2D pore structure by the exclusion of porogenic agent method from magnetron sputtered Bi_2Te_3 films. Reproduced with permission from Ref. [86], © American Chemical Society 2019. (h) The cross-section of the TE PEDOT-Tos/SWCNTs aerogels prepared using freeze-drying method for 2D quasi-ordered pores introduction. Reproduced with permission from Ref. [77], © Elsevier Ltd. 2021. (i) SEM image of the 2D ordered pores in porous graphene films. Reproduced with permission from Ref. [52], © Elsevier Ltd. 2016. (j) Cross-sectional SEM image for 3D disordered pores in Cu_2Se prepared through solid-state explosion reaction combined with SPS CNT foam. Reproduced with permission from Ref. [95], © WILEY-VCH Verlag GmbH & Co. KGaA, Weinheim 2017. (k) The 3D double-interconnected network porous microstructure, where the cross-linked network of SWCNTs is closely attached to the network of rGO nanosheets surfaces. Reproduced with permission from Ref. [78], © American Chemical Society 2017. (l) The 3D lattice for $(Bi, Sb)_2(Te, Se)_3$-based alloys with ordered pore structures constructed by direct ink writing. Reproduced with permission from Ref. [49], © Kim, F. et al. 2021.

system while preserving good electrical properties. The ratio σ to κ for this nanoscale silicon fabric (4000 $C^2 \cdot K \cdot J^{-2}$) is even over three times higher than that of bulk crystalline silicon.

Notably, Fig. 5(f) gives good examples of the introduction for 1D ordered pores in silicon wafer, conducted by Zhang et al. [55]. The metal-assisted chemical etching strategy was employed to fabricate porous silicon nanowire arrays (SiNWAs) with a specific surface area of 547 $m^2 \cdot g^{-1}$. The linear pores are neatly and orderly arranged within the silicon nanowire array, presenting a strikingly symmetrical and ordered distribution. The distinctive morphology of these porous structures endows them with a remarkably high S of 513 $\mu V \cdot K^{-1}$ and an exceptionally low κ of 1.68 $W \cdot m^{-1} \cdot K^{-1}$. Consequently, they achieve a notable ZT value of 0.49 at 300 K, surpassing that of bulk silicon almost two orders of magnitude.

2.2.3 2D pore

2D pores can be described as pores existing in two-dimensional materials, distributed along grain boundaries of layered or thin film materials and within lamellar structures. An instance of a 2D pore structure is encountered in the porous n-type Bi_2Te_3 thin films in the study conducted by Qiao et al. [86]. Introduction of 2D pore structure by the exclusion of porogenic agent from magnetron sputtered Bi_2Te_3 films. Figure 5(g) displays nanopores within the film exhibiting a polyhedral geometry with the irregular distribution in grain boundaries. These pores and highly smooth boundary can strongly scatter phonons, leading to the significant decrease κ_L (the minimum κ_L of 0.36 $W \cdot m^{-1} \cdot K^{-1}$) of the samples.

In the work of Wang et al., a porous PEDOT-Tos/SWCNT TE aerogel with a remarkably high porosity of 95.2% was prepared using freeze-drying method [77]. The characterized pore sizes distribute ranging from 10 to 50 μm. Figure 5(h) illustrates its layered porous structure featuring a "layer–pillar" framework, with interlayer spacing varying from tens of micrometers to one hundred micrometers. It is evident that distribution of pores is in a coexistence of order and disorder in this aerogel. Importantly, this type of porous material can be used to create ultra-light and elastic TEGs demonstrating the potential for heat collection applications, which will be discussed in detail in the following sections. Guo et al. employed the same method to introduce a 2D pore structure into graphene films [52]. Figure 5(i) shows the SEM image of its cross-

section, revealing the pore distribution between lamellars. These pores are orderly arranged between the graphene layers. At the same time, the fast electron transport in the porous graphene film is ensured due to the good contact between the graphene nanosheets. These large-area porous graphene films may be subsequently utilized to fabricate a flexible, lightweight, and stretchable TEG.

2.2.4 3D pore

3D pores refer to large pores in the range of hundreds of nanometers, typically distributed throughout the material in the form of an interconnected network structure. Zhao et al. prepared Cu_2Se bulk samples with 3D pore network structure through solid-state explosion reaction combined with SPS (Fig. 5(j)) [95]. The solid-state explosion reaction results in a highly uniform distribution of grains throughout the sample, with grain sizes in the range of 20–50 nm and pore sizes between 50–200 nm. The limitation of this method lies in its inability to control the distribution of pores, leading to the random dispersion of all pores in the sample. These pores can strongly scatter phonons, significantly reducing κ_L. However, further solutions are needed to address their detrimental effects on the electrical transport properties.

Tan et al. developed rGO/SWCNT hybrid aerogels using the freeze-drying method [78]. The hybrid aerogel exhibits the microstructure of 3D double-interconnected network with a porosity over 99%, as shown in Fig. 5(k). Interestingly, the rGO/SWCNT hybrid aerogels were characterized by ultra-light with an apparent density of 10 $kg{\cdot}m^{-3}$. In this hybrid aerogel of a unique 3D network pore structure, an ultra-low κ_L = 0.021 $W{\cdot}m^{-1}{\cdot}K^{-1}$ is achieved through phonon scattering effects at the pore interfaces. Additionally, the σ increases to 6.66 $S{\cdot}cm^{-1}$, mainly attributed to the 3D interconnected network microstructure.

In fact, for the design of ordered pore structures, direct ink writing is a highly effective method. Kim et al. utilized colloidal inks $(Bi, Sb)_2(Te, Se)_3$ with high viscoelasticity without organic binders to sequentially deposit layers and construct a 3D TE lattice with regularly arranged large pores [49]. These TE particles are solidified well under sintering promotion, forming a robust 3D structure at a macroscopic scale and exhibiting an ordered pore structure at a microscopic scale, as shown in Fig. 5(l). This method enables the rational design of pore structures, providing a new perspective on introducing pores into materials. Similarly, in the work of Choo et al., the construction of three-dimensional honeycomb Cu_2Se TE materials can be achieved through a 3D printing process based on extrusion molding [51]. This design with a periodic pore structure can enhance the mechanical stiffness of the TE module, thereby improving its efficiency and durability, which will be discussed in detail later.

3 Thermoelectric property

Pore engineering has been reported to have a significant contribution for the thermal transport suppression of TE materials [71, 72, 89, 103]. In this section, we first present the fundamental mechanism of the pore structure in detail, i.e., the scattering mechanism, and further introduce it through the phonon gas theory. We then summarize typical improvement strategies, including the combination of pores with various structuring, such as point defects, dislocations, nano-precipitates, grain boundaries, and hierarchical structures. The advanced characteristics of these new structures are concisely introduced through carefully selected examples. Besides, we discuss the challenges and prospects for the future development of pore structures.

3.1 Mechanism and strategy of optimization for κ_L suppression

In pore engineering, the κ_L for the material decreases significantly, which is mainly attributed to the pronounced phonon scattering at pore interface [25, 46, 104, 105]. This phenomenon can be regarded as the predominant mechanism driving the enhancement of TE properties. Notably, the effect of phonons scattering by pores is closely related to their morphology. Namely, pores with various shapes scatter phonons in different directions, leading to diffusive scattering and consequent reduction in κ_L [89]. According to the phonon gas theory, κ_L of the 3D isotropic materials can be written as $\kappa_L = 1/ C_V v l$, where C_V, v, and l represents for the constant volume heat capacity, sound velocity, and phonon mean free path, respectively [95, 106]. The impact of pore structure extends to two additional aspects. On the one hand, the interior of the pore lacks the heat medium because of the vacuum state or gas filled inside it, leading to the slow transmission or even non-transmission of phonons [107]. In this case, the weak transmission of phonons lowers C_V and v, causing a suppression for κ_L. On the other hand, by manipulating the pore intervals, the shortened l for the phonon scattering can suppress the κ_L of materials. In fact, we can have a better understanding of this point through phononic crystals (PnC), an artificial periodic nanostructure. One interesting work was conducted by Zen et al. [108], they designed a square array with ordered circular pores periodically, as shown in Fig. 6(a). The circular pores were chosen to reduce the possibility of cracking. This orderly arrangement of pore structures has been proven to control phonon thermal conductivity using coherent band structures. More specifically, in the work of Li et al. [109], the relationship among the phonon wavelength (λ), l, and the periodicity (a) of the PnC was given. These three parameters are also the three important length scales of the nanophononic crystal (NPC) at the pore boundary, and the specific relationship between them is as follows: (1) when $a < \lambda$, the wave-like phonon interference induced by coherent scattering plays a major role; (2) when $a > l$, particle-like diffusive scattering dominates; (3) when $\lambda < a < l$, there is controversy over the dominance of phonon interference and scattering (Fig. 6(b)). For phonon interference, the reduction of κ is mainly due to the flattening of the phonon band structure, which leads to a reduction in the phonon group velocity. For diffusive scattering, the reduction of κ is due to the decrease in l and lifetime of phonons [110–112]. Experimentally, Nobuyuki et al. carried out the emitted phonon power (P) in membrane with periodic pores below 1 K in Fig. 6(c) [108]. It is found that the structure of ordered pores with a periodic scale > 1 μm significantly reduces the heat transfer. The observed experimental results are in quantitative agreement with the proposed theoretical calculations. This experiment gives direct evidence that phonon scattering is directly related to l.

Note that the mean free range of phonons in solids is distributed over a wide range from the atomic scale to the micrometer scale. However, most of the pores contained in the material are larger than the nanometer size. Consequently, pores in the TE material are often combined with other defects including point defects, grain boundary, nanostructure, mesoscopic precipitates, and pores, to reduce the κ more efficiently. The frequency-dependent spectral

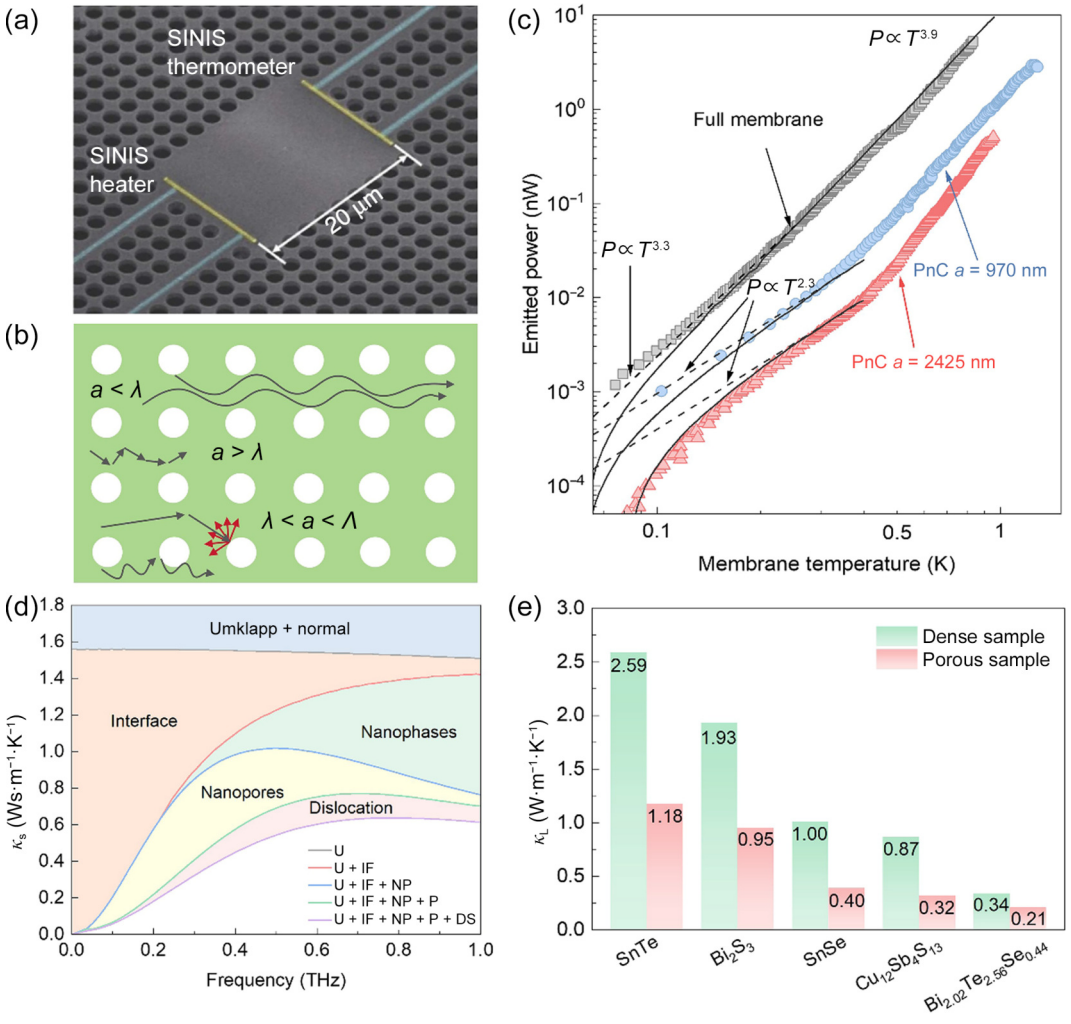

Figure 6 (a) A false color SEM of the central region of the larger period a = 2425 nm PnC sample. The blue (Al) and yellow (Cu) lines are the metallic wiring which forms the heater and thermometer elements at the center of the PnC. The shorter period sample has the same wiring locations and dimensions. The full size of the perforated membrane is 100 μm × 100 μm. Reproduced with permission from Ref. [108], © Zen, N. et al. 2014. (b) The three possible regimes of phonon transport in a 2D NPC, which are determined by the relationship between λ, l, and a of the NPC. Reproduced with permission from Ref. [109], © Springer Nature Limited 2021. (c) At low temperature, the temperature dependence of the conductance is different for the full membrane ($P \propto T^{3.3}$) and for the NPCs ($P \propto T^{2.3}$). Reproduced with permission from Ref. [108], © Zen, N. et al. 2014. (d) Frequency-dependent spectral lattice thermal conductivity of α-MgAgSb sample under 473 K calculated by the Debye–Callaway model, including grain boundaries, nanophases, nanopores, and dislocations. Reproduced with permission from Ref. [113], © Elsevier Ltd. 2023. (e) Comparison of κ_L between dense materials and porous materials at room temperature, including SnTe, Bi_2S_3, SnSe, $Cu_{12}Sb_4S_{13}$, and $Bi_{2.02}Te_{2.56}Se_{0.44}$ [47, 68, 114, 115].

lattice thermal conductivity (κ_s) can be expressed by Eq. (2)

$$\kappa_s = (\kappa_B/2\pi^2 v)\cdot(\kappa_B T/\hbar)^3 \cdot \int_0^{\theta_D/T} \tau_{tot}(x)\, x^4 \exp^x/(\exp^x - 1)^2 \mathrm{d}x \quad (2)$$

$$\tau_{tot}^{-1} = \tau_U^{-1} + \tau_{GB}^{-1} + \tau_{PD}^{-1} + \tau_{PI}^{-1} \quad (3)$$

where κ_B is the Boltzmann constant, $\hbar$ is the reduced Planck constant, θ_D is the Debye temperature, τ_{tot} is the phonon scattering relaxation time, and x is the phonon frequency defined as $\hbar\omega/\kappa_B T$, where ω represents for the phonon frequency. Note that τ_U, τ_{GB}, τ_{PD}, and τ_{PI} denote the relaxation rate for Umklapp, grain boundary, point defects, and pore interface scattering. Figure 6(d) shows the calculated κ_s of Umklapp process (U), IF, nanophases (NP), nanoscale-pores (P), and DS with respect to ω at 300 K. The area under the κ_s curve corresponds to κ_L, attributing to the contribution of the specified defects. The results show that IF scatter low-frequency phonons, P and DS scatter medium-frequency phonons, and NP scatter high-frequency phonons [96, 114, 116, 117]. Rational design and integration of structures with pores benefit the multi-scale scattering of phonons, which significantly contributes to the reduction of κ_L. Figure 6(e) compares the κ_L of a typical TE system at room temperature based on the above strategy, demonstrating an efficient reduction of κ_L. For example, introducing a porous structure in SnTe [114], Bi_2S_3 [68], SnSe [115], and $Cu_{12}Sb_4S_{13}$ [47] combined with other defects and even multi-scale hierarchical structures significantly reduces κ_L to 1.18, 0.95, 0.40, and 0.32 W·m^{-1}·K^{-1} by more than 50% compared to that of dense samples for 2.59, 1.93, 1.00, and 0.87 W·m^{-1}·K^{-1}, respectively.

3.2 Thermal property

For porous TE materials, the effect of pore size on the κ_L is very important. In this regard, the research of Kimberly et al. provide a good example of how the pore size regulates the κ_L. They successfully prepared Bi_2Te_3 with Kirkendall nanopore by solution-based method shown in Figs. 7(a) and 7(b). As the pore size increases from 16 to 50 nm, κ_L monotonically decreases to

0.21 W·m^{-1}·K^{-1} for the vertical direction (Figs. 7(c) and 7(d)) [118].

As discussed above, constructing various defects can scatter phonons for various frequencies to reduce κ_L of TE materials. One example is that in porous $Bi_2Te_{2.5}Se_{0.5}$ samples with the porosity over 20% produced by hollow nanorods, a significant abundance of grain boundaries and dislocations is present. Figure 7(e) shows the sintered sample with the large flake grains and embedded 1D disordered pores with 1 μm of width among the grains. Furthermore, the grain boundaries between the grains are well bonded (Fig. 7(f)), ensuring the electrical transport behavior and mechanical strength of the material. A large number of dislocations with density of 5.0 × 10^{11} cm^{-2} also can be captured giving in Fig. 7(g). Due to the broad-range phonon frequency scattering and the large porosity, the respective κ_L is effectively reduced to 0.2 and 0.14 W·m^{-1}·K^{-1} at 300 and 550 K (Fig. 7(h)), while the ZT value reaches a maximum of 1.18 at 463 K [99]. Similarly, the 0D porous structure combined with high density of dislocations and grain boundaries was introduced in the n-type Cl-doped Bi_2S_3. Due to the

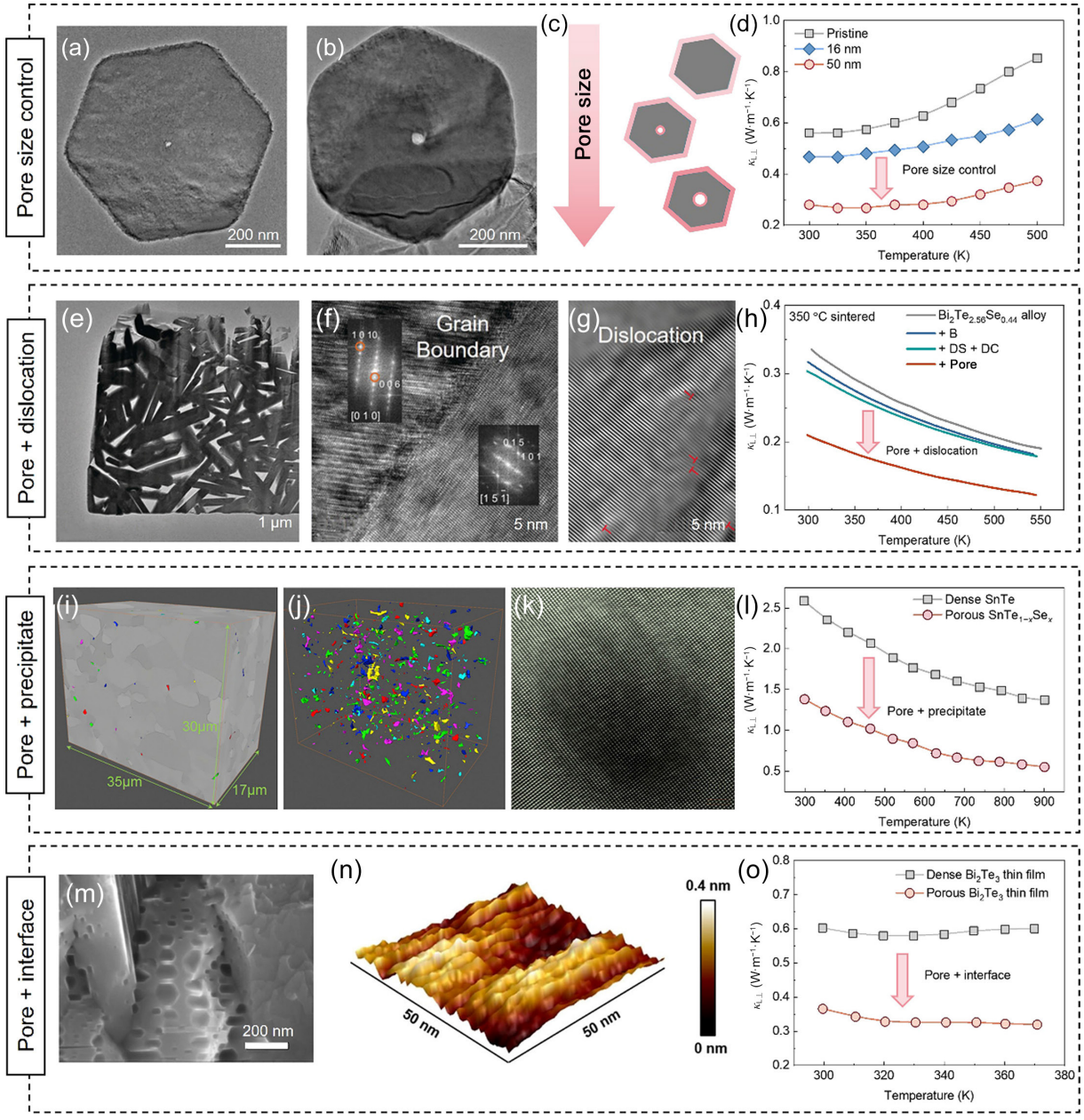

Figure 7 Transmission electron microscopy (TEM) micrograph of Bi_2Te_3 nanoplates with (a) small pore of 16 nm and (b) large pore of 50 nm. (c) Schematic diagram of pore regulation. (d) Temperature-dependent κ_L in the perpendicular direction for Bi_2Te_3 nanoplates with a single nanopore. Reproduced with permission from Ref. [118], © Kimberly, T. Q. et al. 2024. (e) TEM image of the porous $Bi_{2.02}Te_{2.56}Se_{0.44}$ nanocomposite. (f) High-resolution TEM (HRTEM) image showing a grain boundary. (g) Inverse fast Fourier transform (IFFT) of a HRTEM image showing dislocations. (h) Theoretical modeling of κ_L of the 350 °C-sintered BiTeSe nanocomposite. Reproduced with permission from Ref. [99], © Wiley-VCH Verlag GmbH & Co. KGaA, Weinheim 2017. (i) 3D back-scattered SEM image of sintered $Sn_{0.96}Cd_{0.08}Te_{0.88}Se_{0.12}$ and (j) accordingly determined pores distributions. (k) HRTEM image for a typical nanoprecipitate coherently embedded in the matrix. (l) Temperature-dependent κ_L of dense and porous SnTe. Reproduced with permission from Ref. [114], © Elsevier Ltd. 2019. (m) Cross-sectional SEM image of nanopores for porous Bi_2Te_3 thin film. (n) Atomic force microscopy (AFM) image of the nanopore boundary showing a roughness of 0.4 nm. (o) Temperature-dependent κ_L of dense and porous Bi_2Te_3 thin film. Reproduced with permission from Ref. [86], © American Chemical Society 2019.

synergetic phonon scattering by pore interfaces and the above defects, the minimum κ_L of the porous sample reduces to 0.36 W·m^{-1}·K^{-1} at 823 K, which is about 35% lower than that of the dense sample. Therefore, Bi_2S_3 achieves a record maximum ZT value of 0.81 at 823 K [68]. Apart from these examples, the SnSe with nanopores is fabricated by *in situ* decomposition of $InSe_y$ nano-precipitates embedded in the matrix during the sintering process. The introduction of pore structures, effectively impedes the transmission of phonons, thereby achieving an exceptionally low κ of 0.24 W·m^{-1}·K^{-1} at 823 K [115].

Figures 7(i) and 7(j) display an example that fabricated porous $SnTe_{1-x}Se_x$ with the majority of pores being less than 200 nm. Additionally, Cd-rich nano-precipitates also can be observed embedding in a matrix as a coherent interface (Fig. 7(k)), while geometric phase analysis (GPA) demonstrated a significant strain between the matrix and the nano-precipitates. The observed multi-scale hierarchical structures including nanoscale precipitation, pores, and grain boundaries effectively scatter the phonon and reduce the κ_L of $SnTe_{1-x}Se_x$. The κ_L decrease from 1.37 to 0.53 W·m^{-1}·K^{-1} under 900 K (Fig. 7(l)) and thus leading to a boosting ZT over 1.5 at 900 K [114]. Another representative work is the 3D pore network forming in the tetrahedrite $Cu_{12}Sb_4S_{13}$-based materials by the addition of BiI_3 sublimation. In addition, the hierarchical structure in the material also includes point defects, dislocations, second phases, and lattice strains. Consequently, the synergistic effect of these structures leads to a remarkable 72% reduction in κ_L of 0.14 W·m^{-1}·K^{-1} and an increased ZT value of 1.15 at 723 K [47]. Moreover, Chen et al. employed a hierarchical structure consisting of pores, a metastable phase, nanosized grains, semi-coherent grain boundaries, and high-density dislocations with localized strains in β-Ag_2Se achieving an incredibly low κ_L of 0.35 W·m^{-1}·K^{-1} at 300 K [72].

Actually, besides applying pore engineering in bulk materials, introducing pore structures in thin films also has great benefits for optimizing TE performance. Qiao et al. initially prepared Bi_2Te_3 films through magnetron sputtering, and subsequently introduced pore structures using the exclusion of porogenic agent technique. The resulting sample exhibited faceted-shaped pores (Fig. 7(m)) with highly smooth boundaries of a roughness of 0.4 nm in Fig. 7(n). As a result, the unique structure effectively scatters phonons, leading to a significant reduction in κ_L to 0.36 W·m^{-1}·K^{-1} (Fig. 7(o)). Remarkably, a maximum ZT value of approximately 0.67 is successfully achieved at room temperature, even being comparable to commercial bulk TE materials [86]. Recently, 3D porous MoS_2/CNTs films have been prepared by freeze-drying method, showing a remarkable efficiency for hindering heat transfer. Consequently, the film attains a low κ of 0.019 W·m^{-1}·K^{-1}, resulting in a corresponding ZT value of 0.17 at room temperature. Notably, this ZT value is 65 times higher than that of a pure MoS_2 film [119]. In addition, the composite of CNTs not only increases the interfacial scattered phonons and thus enhances the ZT for porous film, but also effectively improves the tensile strength of the film.

3.3 Electrical property

It is noteworthy that the decrease in κ cannot adequately compensate for the loss of σ when pores are present exclusively within the material [54, 120, 121]. As a result, further exploration is required to improve the TE properties through the development of a hierarchical system or other innovative approaches. More details regarding electrical properties will be explained in this section.

Although the pore structure contributes a lot to the reduction of κ, it also has a significant negative impact on electrical performance. In our analysis of electrical properties, we primarily focus on the power factor (PF). Firstly, the existence of pores introduces boundary barriers and impedes charge transport, leading to reduced carrier mobility (μ) and a consequent decrease in conductivity [69, 85, 122, 123]. Secondly, the interface of pores plays a positive role in the enhancement of S because of the carrier scattering. The equation for the single parabolic band (SPB) expression of the Seebeck coefficient is expressed as [124]

$$S = \left(8\pi^2\kappa_B^2/3eh^2\right)\cdot m^*\cdot T\cdot\left(\pi/3n\right)^{2/3}\cdot(1+R) \quad (4)$$

where e, h, m^*, n, and R represents for the electronic charge, Planck constant, effective mass, holes concentrations, and scattering parameters, respectively. The R can be expressed as

$$R = \left(\mathrm{d}\ln\lambda_s/\mathrm{d}\ln E\right)_{E_f} \quad (5)$$

where λ_s, E, and E_f represents for the scattering distance, average energy of electrons, and the Fermi energy, respectively [125]. Normally, the enhancement of S can be achieved through introducing additional scattering centers, such as ionized impurities. Additionally, the presence of pores increases the scattering exponent, thereby improving S. Note that an intrinsic coupling exists between σ and S as two important parameters of the electrical transport behavior regarding carrier concentration n and mobility μ [99]. Several solutions have been proposed to solve the problem, and some examples are given to illustrate it as follows.

Based on pasted experience, if the pore spacing is longer than l of carriers and shorter than phonons, the κ_L will be greatly reduced with little effect on the electrical conductivity. Normally, introducing small-scale pores in the material contributes to optimizing charge transfer. For example, the introduction of Cl into Bi_2S_3 leads to the shifting of the Fermi level towards the conduction band transforming it into a degenerate semiconductor and increasing its n, as shown in Fig. 8(a). This effectively enhances the σ for TE semiconductor even though the decrease of μ caused by nanopore structure and grain boundaries. Based on elevated σ, the PF of Cl-doped Bi_2S_3 sample with nanopore accordingly reaches 4.7×10^{-4} W·m^{-1}·K^{-2}, which is 9.4 times higher than that of pure Bi_2S_3 (Fig. 8(b)). Importantly, the resulting Bi_2S_3 with nanopore achieves its highest recorded ZT value of 0.81 at this specific temperature for the first time [68]. To better form conductive pathways in porous materials for efficient charge transport, Li et al. give a good example of introducing a 3D conductive network in a porous $Bi_2Te_{2.7}Se_{0.3}$ (BTS) as depicted in Fig. 8(c). Its interface of network is a sandwich-like structure composed of pore-CNT-BTS atomic layers, which can maintain the charge transport due to the conductive CNT-BTS layers and simultaneous effective scattering phonons by the pore-CNT interface. In addition, the introduction of the aforementioned conductive network also improves the S of −161 μV·K^{-1} (Fig. 8(d)). Therefore, this hybrid exhibited an impressive PF of 22 μW·cm^{-1}·K^{-2}, resulting in a high ZT value of approximately 1.2 at 450 K [107]. Apart from the mentioned two strategies, the electrical performance of porous materials can be further enhanced by incorporating carbon fibers or graphite [126]. Additionally, it is necessary to explore more strategies for the improvement.

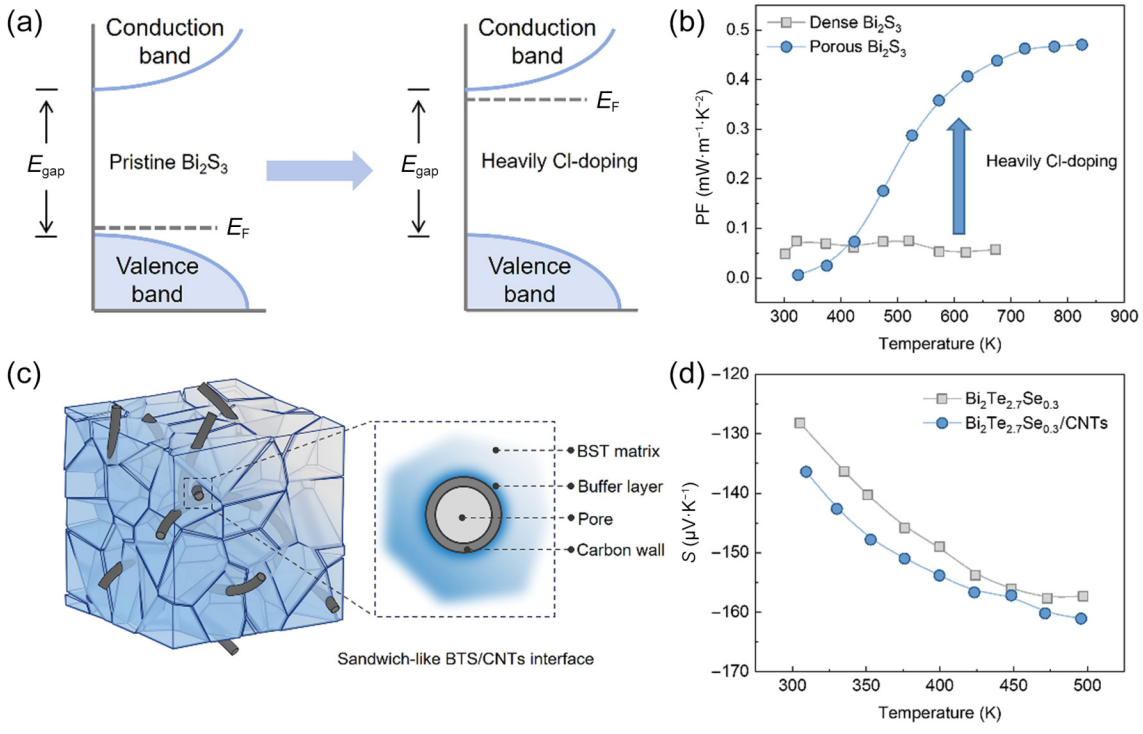

Figure 8 (a) Schematic diagram of optimization of electron transport through band engineering. Fermi level rising into conduction bands increases carrier concentration. (b) Temperature-dependent power factor of porous Cl-doped Bi_2S_3 and pure Bi_2S_3. (c) Schematic illustration of 3D atomically thin conductive framework in porous BTS/CNTs to improve electrical properties. (d) Temperature-dependent *S* of $Bi_2Te_{2.7}Se_{0.3}$ and $Bi_2Te_{2.7}Se_{0.3}$/CNTs. Reproduced with permission from Ref. [107], © WILEY-VCH Verlag GmbH & Co. KGaA, Weinheim 2020.

3.4 Decoupling of thermoelectric parameters

Note that the presence of pores in solids influences both charge and thermal transport simultaneously. The most important function of the pores is the scattering of phonons to reduce the κ_L. Meanwhile, this lattice-pore interface also inhibits charge transport and thus reduces mobility (μ_H), which is detrimental to thermoelectric materials. These two opposite factors give a physical coupling of the thermoelectric parameters. To maximize the thermoelectric performance of materials, a key focus in thermoelectrics has been the development of strategies to mitigate the strong correlation between μ_H and κ_L [127]. Consequently, enhancing the ratio of μ_H to κ_L plays a crucial role in optimizing thermoelectric materials, often quantified by the quality factor (*B*) given in Eq. (6) [128]

$$B = 9\frac{\mu_W}{\kappa_L}\left(\frac{T}{300}\right)^{5/2} \quad (6)$$

where μ_W represents for weighted mobility, which is positively correlated with μ_H.

To gain higher quality factor *B* in porous thermoelectric materials, by two factors need to be involved. For one thing, the morphology of the pores should be carefully designed including size, concentration, distribution, etc., to ensure charge transport while scattering phonons. For example, the porous poly(2-(2-decyltetradecyl)-5-dodecyl-6-(5-(selenophen-2-yl)thiophen-2-yl)-3-(thiophen-2-yl)-2,5-dihydropyrrolo[3,4-c]pyrrole-1,4-dione) (PDPPSe-12) film exhibits an increased *B* value of 1.3×10^3 compared with that of the dense sample (0.8×10^3) at 300 K [129]. The Bi_2Te_3 thin film with nanoporous displays an improved *B* approximately 1.3 times from 3.5×10^3 to 4.7×10^3 with the increasing porosity from 0% to 6% [86]. However, when the porosity is over 10%, the *B* value decreases drastically to 2.9×10^3. On the other side, the strategy for pores introduction needs to cooperate with other strategies, to compensate for the electrical properties. Based on these designs, many cases have achieved high *B* values via pore construction. The pore engineering strategy implemented in PbSe system is a typical example [85]. PbSe is optimized by joint strategies for the pore and carrier engineering exhibiting *B* value of 4×10^3, which is higher than those of $Pb_{0.9975}Sb_{0.0025}Se$ and $Pb_{0.9975}Bi_{0.0025}Se$ (3×10^3) for single carrier engineering, $Pb_{0.95}Sb_{0.033}Se$ (1×10^3) for defect engineering, and comparable for those of PbSe-Br and $PbSe_{0.8}Te_{0.2}$-Br [130–132]. However, because of the single scattering mechanism for pore, the effect is limited on decoupling thermoelectric parameters compared to finer chemical compositional modulation strategies (*B* value over 6×10^3). The thermoelectric properties of part of TE materials are presented in Table 1 for the convenience understanding of pore strategy.

4 Mechanical property

TE materials are generally composed by ionic bonds, such as PbTe [133, 134], Bi_2Te_3 [15], $CoSb_3$ [135], Ag_2Se [6], etc., exhibiting brittle properties. The introduction of pore structure is one way to enhance flexibility, which refers to the ability of a material to deform without breaking. Designing and constructing the appropriate pore structure in the TEs can reduce the density and regulate mechanical properties, including strength, plasticity, and elasticity. Note that Ag_2Se is a typical brittle TE semiconductor [136]. Liu et al. successfully fabricated a Ag_2Se 3D network (Fig. 9(a)) with a large size of 1.8 m × 0.9 m through two-step impregnation method [137]. It is the reticular construction that provides a superior elasticity for it and the pore structure

Table 1 Thermoelectric properties for porous system with 0D to 3D pore

Material	Pore structure type	σ (S·cm^{-1})		S (μV·K^{-1})		κ (W·m^{-1}·K^{-1})		κ_L (W·m^{-1}·K^{-1})		ZT		Temperature (K)	References
		Dense	Porous	Dense	Porous	Dense	Porous	Dense	Porous	Dense	Porous		
Cl-doped Bi_2S_3	0D	102	92	−222	−232	0.86	0.48	0.49	0.36	0.48	0.81	823	[68]
PbS		475	403	−186	−186	1.45	1.10	—	0.56	0.94	1.07	838	[98]
SnSe		70	45	287	296	0.43	0.22	0.34	0.16	1.26	1.71	823	[115]
α-MgAgSb		5	5	208	208	0.93	0.73	0.55	0.36	1.12	1.36	473	[113]
Bi_2Te_3 (⊥)		235	500	−196	−146	0.76	0.62	0.67	0.27	0.47	0.74	423	[118]
Bi_2Te_3 (//)		469	699	−202	−128	1.88	1.48	1.53	0.94	0.44	0.34	423	
$Bi_2Te_{2.5}Se_{0.5}$	1D	717	520	−186	−127	1.16	0.48	0.40	0.14	1.10	1.18	463	[99, 101]
silicon		—	132	—	382	—	1.68	—	—	—	0.493	300	[55]
Bi_2Te_3	2D	1237	699	−120	−153	1.44	0.85	0.60	0.39	0.71	0.51	370	[86]
PEDOT-Tos/SWCNTs		4.3	2.5	50	48	0.25	0.09	—	—	0.98	0.82	300	[77]
Cu_2Se		130	310	296	232	0.74	0.91	0.55	0.42	1.91	1.51	1000	[95]
rGO/SWCNT	3D	—	7	—	29	—	0.02	—	—	—	0.008	300	[78]
$Bi_{0.5}Sb_{1.5}Te_3$		—	454	—	214	—	0.80	—	—	—	0.99	373	[49]
$Cu_{12}Sb_4S_{13}$		604	542	150	155	1.28	0.82	0.53	0.14	0.78	1.15	723	[47]
SnTe		703	443	158	207	2.45	1.27	1.39	0.55	0.66	1.72	900	[114]
PbSe		460	270	−190	−216	1.41	0.96	0.80	0.56	0.96	1.15	823	[85]

deformation helps a lot to the engineering stretching and compressing of the Ag_2Se network. An excellent tensile strain (ε_t) of > 100% and a compressive strain (ε_c) of > 80% were obtained, as shown in Fig. 9(b). From the compressive stress–strain curve, the Young's modulus of the Ag_2Se network is extracted of 0.03 MPa. Very importantly, this ultra-low Young's modulus is considered as an ideal and tissue-like modulus that enables the intimate fitting of devices with the uneven skin, reducing the effects of mechanical loads. Figure 9(c) displays a photograph of a network-based flexible TEGs (FTEG) worn on the arm, showing that the surface of the Ag_2Se network fits well to the human skin. Due to the excellent flexibility of networked FTEGs, this could lead to the implementation of FTEGs in real-world applications such as partial fillers in commercial jackets (Fig. 9(d)). This work demonstrates that the brittle TE semiconductors can be transformed into flexibility by the introduction of pore structures.

Similarly, Li et al. fabricated n-type TE fibers with 3D interconnected porous structures through wet spinning process (Fig. 9(e)) [52]. It is precisely because of this interconnected structure that the fiber has excellent mechanical strength and stretchability. Its tensile elongation is as high as 434%, and its breaking stress is 11.8 MPa, which remains at a relatively high level, as shown in Fig. 9(f). This excellent mechanical strength and stretchability enable the fiber to withstand a cumulative weight of 100 g, which is more than 5500 times of its own weight. The other example is the porous microstructured ultralight aerogel with a skeleton composed of SWCNT, PEDOT-Tos and insulating cellulose interconnected by a freeze-drying process in the work of Chen et al. [77]. Its pore size distribution histogram shows that 82.4% of the pores are between 10 and 50 μm. The mechanical stability of the aerogel was confirmed by cyclic stress–strain testing. After repeated compression for 1–5 cycles under different strains, the maximum stress value can be basically restored. This provides a strategy for future application scenarios under compression environments.

Inspired by natural world, Jae Sung Son et al. [51] used direct ink writing technology to prepare a Cu_2Se TE module with a 3D honeycomb structure (Fig. 9(g)). They used the Ashby–Gibson relation to predict the compressive stiffness of the Cu_2Se honeycomb structure, shown in Fig. 9(h). The effective density of the honeycomb structure is only 600–1000 kg·m^{-3}. By comparing with other common materials with a density close to 1000 kg·m^{-3}, the Cu_2Se honeycomb structure exhibits a specific stiffness of 198 kPa·m^3·kg^{-1}, which is 2 times higher than others with high specific stiffness. This strategy of designing structures that simultaneously reduce density and enhance specific stiffness brings broad prospects for the development and application of TE devices. Very importantly, although many existing strategies such as doping, entropy engineering, defect engineering, etc., achieved significant results in decoupling the thermoelectric parameters, they contribute rarely to the improvement of mechanical properties. In contrast, the construction of porous structures optimizes the strength and also confers more mechanical functionality in given technology.

Importantly, using direct ink writing technology enables more precise design and construction of the pore structure to realize a broader range of mechanical functions such as compliance. For example, Karthikeyan et al. [138] demonstrate an approach to potentially enhance the power conversion efficiency while suppressing the brittle failure in TE materials employing direct ink writing technology to fabricate microlattices. The resulting microlattices, with a hybrid carbon core and a TE thin film shell, demonstrate a significantly enhanced compressive modulus of 450 MPa and a strength of around 35 MPa. Additionally, these TE microlattices exhibit localized plastic buckling over 50% of strain without any noticeable strut fractures upon yielding, as depicted in Fig. 9(i). Note that the property of compliance is ability of a material or structure to deform in response to an applied force. It requires more deformability than flexible materials. More importantly, TE devices constructed with these microlattices exhibit excellent conformability, which can convert the energy thermoelectrically on the surfaces of complex components (Fig. 9(j)).

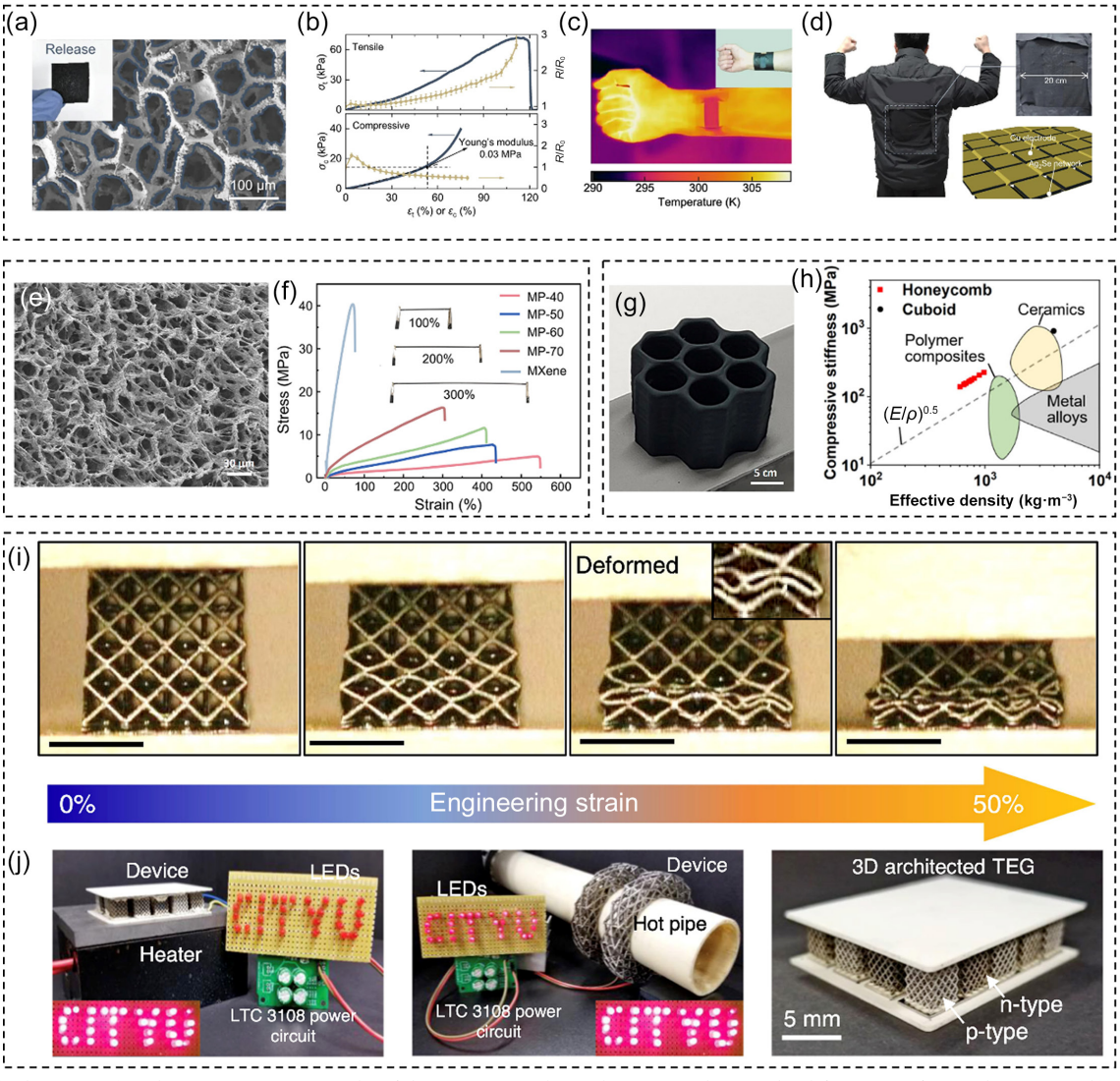

Figure 9 (a) Photos (inset) and cross-section micrographs of the Ag_2Se network in release states, showing the deformation of network structure. (b) Tensile stress (σ_t)–strain (ε_t) curve and compressive stress (σ_c)–strain (ε_c) curve with corresponding resistance change (R/R_0, where R and R_0 represent the resistance after and before the deformation). (c) The infrared image and optical photograph (inset) of a network-based FTEG dressed on a human wrist. The top electrode was removed to avoid the effect caused by its low emissivity. (d) A thermoelectric jacket filled with the Ag_2Se network-based FTEG. Reproduced with permission from Ref. [137], © Liu, Y. J. et al. 2023. (e) SEM image showing homogeneous and sparse porous structures in the $Ti_3C_2T_x$ MXene nanoflakes and polyurethane fibers. (f) Tensile–strain-dependent stress curves of MP fibers with different MXene contents. Reproduced with permission from Ref. [48], © American Chemical Society 2023. (g) Schematic for the Cu_2Se-based honeycomb cellular architecture by using all-inorganic $Cu_{2-x}Se$ ink. (h) Compressive stiffness–density Ashby plot showing the cellular Cu_2Se materials described in this paper compared with other materials. Reproduced with permission from Ref. [51], © Choo, S. et al. 2021. (i) Deformation behavior of the TE microlattices under uniaxial compression (scale: 5 mm). (j) Conformability of the developed 3D architected TEGs to conform to any desired surface. Reproduced with permission from Ref. [138], © Karthikeyan, V. et al. 2023.

5 Device design and application

5.1 Device design

TE devices are typically composed of a structured arrangement of TE materials, designed to convert heat into electrical energy [139, 140]. For optimal performance, these devices should be highly efficient in energy conversion, which demands materials with a high ZT [141, 142]. Flexibility is also critical for revolutionary devices, especially for applications involving curved or irregular surfaces, which necessitates the use of flexible materials that can withstand mechanical deformation without losing functionality [143]. For wearable self-generating, devices not only require a flexible fit to the skin, but also need to be conformable for joint and muscle movements such as bending, stretching, twisting, etc. [144, 145]. Namely, the compliance is necessary for wearable self-generating. Additionally, lightweight construction is essential to reduce the overall mass and improve the integration of these devices into various systems [146, 147]. In this section, we summarize the design of novel TE devices in terms of high efficiency, flexibility, compliance, and lightweight to provide a more complete understanding of the subsequent development of the devices.

5.1.1 *High efficiency*

The fundamental unit of a TEG is a thermocouple circuit consisting of an n- and a p-type TE semiconductor connected by wires [148]. For higher output, multiple such thermocouples are series-

connected and sandwiched by a robust ceramic substrate for protection (Fig. 10(a)) [149]. In the design process of TEG, the selection of the material for the thermocouple component is particularly important for the power generation/cooling efficiency [150, 151]. The introduction of pores and nanostructures in TE materials can serve to decouple the TE parameters and enhance the ZT, and therefore can intensify the energy conversion of TEGs. For example, the complex nanostructures with ultrafine grains and multiscale pores in α-MgAgSb significantly reduce κ_L of 0.46 $W \cdot m^{-1} \cdot K^{-1}$ at 300 K with minor effects on electrical transport. This leads to a high ZT value of 0.94 at 300 K and a ZT_{ave} of 1.16 (300–473 K). Using high-performance α-MgAgSb, a Peltier module was fabricated, achieving an impressive coefficient of performance (COP) of 8.3 at 300 K with a the maximum temperature gradient (ΔT_{max}) of 52 K (Fig. 10(b)) [113].

Guo et al. [52] prepared a high-flexibility graphene film with unique 3D porous structure using freeze-drying method. The 3D pore structure significantly reduces the κ while the interconnected netlike structure composed of graphene nanosheets ensures rapid transport capability of charge carriers, thus achieving synergistic optimization of TE performance. Furthermore, they fabricated a TEG with 10 legs, which achieved an output voltage of 0.43 μW at a temperature gradient of 75 K. Importantly, this large-area porous graphene TEG also exhibits good heat resistance and such a microstructure design provides a new strategy for the efficient design of stretchable, flexible, and lightweight TEGs.

5.1.2 *Flexible*

Traditional TE materials are typically rigid inorganic materials, which makes it difficult fit to complex heat sources in practical applications, such as the human body surface or heat source pipes with complex curvature changes [157–160]. Therefore, developing flexible TE materials and TEG is an urgent challenge, especially in the fields of artificial intelligence and wearable devices.

Currently, research on flexible TE technology is primarily focused on (1) integrating brittle inorganic TE materials into flexible substrates or fillers, and (2) on designing and synthesizing intrinsic flexible TE materials. For the former, Jung et al. have constructed a flexible TE module by inserting porous polydimethylsiloxane (PDMS) sponge into the n- and p-type TE legs of Bi_2Te_3, displayed in Fig. 10(c) [153]. This polymer filler not only serves as a structural support to provide strength, but also demonstrates excellent mechanical flexibility. Through non-periodic bending tests, this TE module can be bent repeatedly over 2000 times with extraordinary flexural strength. It is worth noting that the porous structure of the PDMS filler can effectively reduce κ in the filler region (κ of 0.08 $W \cdot m^{-1} \cdot K^{-1}$), thereby the TE module achieving a higher temperature gradient (ΔT) and output of direct current (DC) voltage.

Although TEG based on semiconductor/polymer composites have achieved flexibility, their instability at high-temperature is not sufficient for many application scenarios. Therefore, exploring intrinsic flexible TE materials is necessary. In this regard, Li et al. prepared a hybrid molybdenum disulfide (MoS_2)/CNTs porous film using freeze-drying method, as shown in Fig. 10(d) [117]. The tensile stress of this film is as high as 38.9 ± 0.2 MPa. The TE wristband made from this film achieved an output voltage of

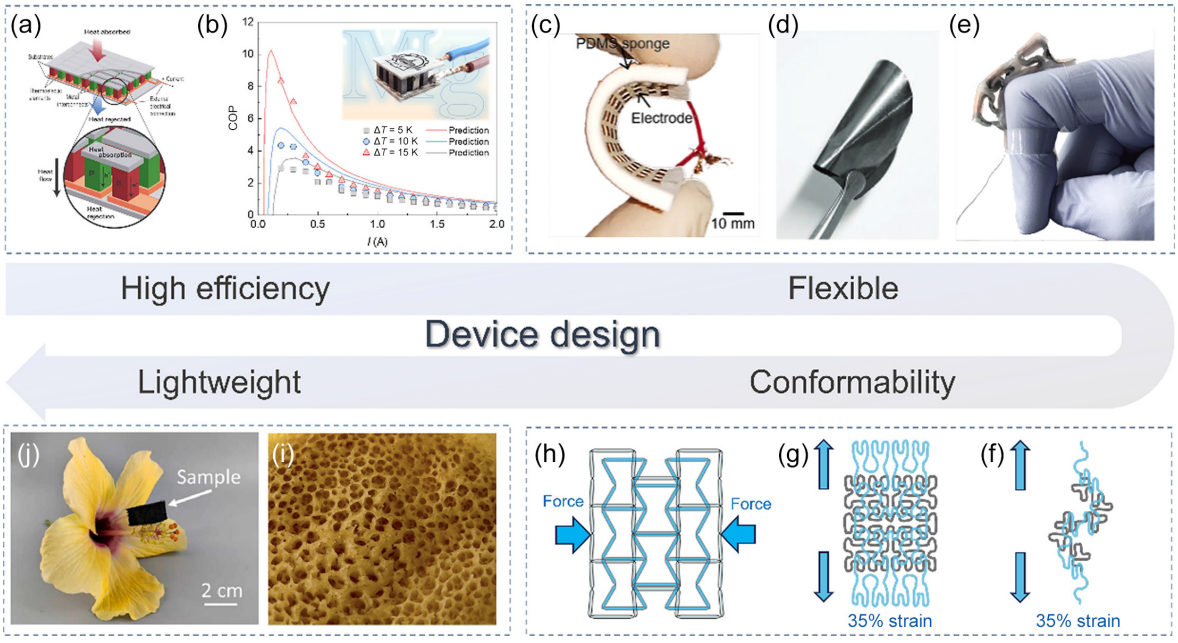

Figure 10 (a). Basic structures of TEG elements. Reproduced with permission from Ref. [152], © IEEE 2018. (b) Current dependent cooling coefficient of performance COP at the hot-side temperature (T_h) = 300 K. Reproduced with permission from Ref. [113], © Elsevier Ltd. 2023. (c) A photographic image of the flexible TEM based on porous PDMS filler. Reproduced with permission from Ref. [153], © Elsevier Ltd. 2020. (d) A photograph of an as-prepared hybrid MoS_2/CNTs film. Reproduced with permission from Ref. [119], © WILEY-VCH Verlag GmbH & Co. KGaA, Weinheim 2020. (e) Photos showing the bending of the S-TED at various angles. Reproduced with permission from Ref. [154], © Elsevier Ltd. 2021. Representative fractal-inspired layouts for hard-soft materials integration, two different patterns for (f) von Koch and (g) Moore curve of metal wires fully bonded to elastomer substrates demonstrate the application of deterministic fractal designs as general layouts for stretchable electronics. In all cases, arc sections replace the sharp corners from the mathematically defined fractal layouts to improve the elastic mechanics. Reproduced with permission from Ref. [60], © Springer Nature Limited 2014. (h) The schematic diagram of auxetic metamaterials before (blue) and after (gray) longitudinal stretching. Reproduced with permission from Ref. [155], © Macmillan Publishers Limited 2017. (i) The pore structure showing the lightweight property of the material. Reproduced with permission from Ref. [156], © Macmillan Publishers Limited 2017. (j) An ultralight TE aerogel standing on stamens of yellow flower. Reproduced with permission from Ref. [77], © Elsevier Ltd. 2021.

2.9 mV and an output power of 0.22 μW under a temperature gradient of 5 K.

However, due to the difficulty of stacking this thin film material to the millimeter-scale thickness, it can only generate the in-plane DC voltage, making it challenging to manufacture vertical-type generators [161]. Therefore, to achieve waste heat recovery of the flexible thin film material under vertical temperature gradients for cross-plane TEG, it is necessary to combine the structural design. Lv et al. proposed a three-dimensional spring-like TE device (S-TED), as shown in Fig. 10(e). The TE module consists of PDMS as the upper and lower support layers (i.e., dual elastomeric connecting layers), multiple rows of parallel serpentine p- and n-type SWCNT films, and air gaps serving as effective thermal insulation layers [154]. This rational design not only greatly enhances the flexibility and compressibility of S-TED but also strengthens the contact between the TE device and the interface, improving the efficiency of energy transfer from the skin to the device. This innovative device design concept provides new ideas for the development of wearable TE devices in the future.

5.1.3 *Conformability*

Note that conformability is that the ability of a material to adapt and closely fit onto irregular or curved surfaces, ensuring good contact without significant gaps. Importantly, the conformability of TEGs is a higher requirement for flexible devices [162]. For wearable TEGs, it is not only required devices to be bendable, but also more complex deformations, such as stretching, bending, and twisting, to ensure complicated movements in following muscles and joints [163, 164]. To achieve such a purpose, the structural conformability is crucial for the TE materials, electrodes, and substrate. A good example is the TEGs of microlattices fabricated by the direct ink writing technique presented in Fig. 9(f). It exhibits a very favorable conformability clinging to the shaped surfaces. Fan et al. [60] proposed a more advanced fractal design for TE devices, inspired by the concept of geometric fractals such as von Koch and Moore curve illustrated in Figs. 10(f) and 10(g), respectively. The reliability of this structure was verified through experimental verification using finite element analysis. This fractal design enables the device to adapt to enhanced elastic strains along the selected dimensions and support biaxial, radial, and other deformation modes. This fractal design concept is proposed to provide strategies for better tissue conformity not only for the structure of TE devices, but also for the electrodes and substrates. Furthermore, as the mechanisms are composed of flexible hinges and rigid elements, the geometric shape of the connecting elements can be designed to make the mechanical device conformable. For example, through a design pattern of inverted hexagons, auxetic metamaterials can be generated, namely materials with tunable Poisson's ratio, as shown in Fig. 10(h) [164]. The shape of this material before and after longitudinal stretching is represented by blue lines and gray lines, respectively. This provides a new approach for device conformability.

5.1.4 *Lightweight*

Lightweighting is critical in the design of TE materials, especially for applications like space exploration and wearable technologies [154, 165, 166]. For the former, reducing the weight of RTGs improves efficiency and payload capacity, while for the latter, lightweight materials enhance comfort and usability. Introducing a porous design effectively reduces the material's weight while maintaining high functional performance, allowing for both improved mechanical flexibility and energy efficiency in these demanding applications (Fig. 10(i)). For example, He et al. [167] fabricated porous BST samples with pore sizes ranging from 1.8 to 20.4 nm (density of 2.1 g·cm^{-3}), by utilizing the principle of 3D printing which employs the optical equipment for layer-by-layer curing and annealing. This rigid sample with extremely low density presents a novel approach and solution for the development of low-cost TE materials. Wang et al. [77] prepared an elastic PEDOT-Tos/SWCNT TE aerogel using freeze-drying technology, with a high porosity of up to 96.4% and pore sizes distributed in the range of 10–50 μm. This ultra-high porosity enables it to exhibit extremely light characteristics, and it can easily stand on a flower petal without causing any damage or deformation to the delicate flower, as shown in Fig. 10(j). Based on the TE aerogel with lightweight and compressibility, an elastic TEG composed of vertically arranged aerogel legs was successfully fabricated for the first time. Under a 50% strain and a temperature gradient of 50 K, it achieved an output power of up to 1967 nW. Similarly, Li et al. [168] employed directional freeze-casting to produce an ultra-light, wood-like aerogel with excellent mechanical and TE properties, possessing a density of 7.5 mg·cm^{-3}. This highly lightweight and compressible TEG can effectively harvest heat under mechanical deformation conditions, such as on the hot plate or compression by human body.

5.2 Application

TE materials enable the direct conversion of temperature differences into electrical energy, making them valuable for energy harvesting [57, 138]. By introducing the porous structure, these materials can be significantly lightweight, enhancing their flexibility and making them suitable for wearable applications. This combination of lightness and wearability opens up potential uses across various fields, such as self-powered health monitoring devices, portable electronics, and even aerospace applications, where efficient, lightweight energy conversion systems are crucial. Here, we summarize some potential application scenarios for porous TEGs.

5.2.1 *Accelerated wound healing for medicine*

Full-thickness wounds often heal slowly or incompletely, leading to significant physical and emotional challenges for patients and costing over ten billion dollars annually for treatment [169]. Traditional wound dressings mainly protect against environmental contamination, supporting a contraction-dominated healing process rather than actively promoting wound closure [170, 171]. In contrast, exogenous electrodynamic fields can enhance the healing process by mimicking the body's natural electric fields, stimulating angiogenesis, cell migration, and proliferation, thereby accelerating tissue repair and regeneration [172–174]. Very recently, Zhang et al. [59] developed a self-powered, flexible, and biocompatible TEG that converts the ambient heat from the skin into microvolt-level electrical energy. This energy activates and upregulates Piezo1-mediated pathways related to tissue regeneration, accelerating *in vitro* cell migration and proliferation, and speeding up *in vivo* wound healing by 4 days. Importantly, this TE device promotes rapid wound healing without the need for amplifiers or additional circuits. These advantages open new interdisciplinary applications for TE technologies and redefine the design of self-powered wearable bioelectronic devices (Fig. 11(a)). On the other hand, Logothetis et al. presents the development of a thermoelectric heat patch for melanoma excision wound care, designed to maintain

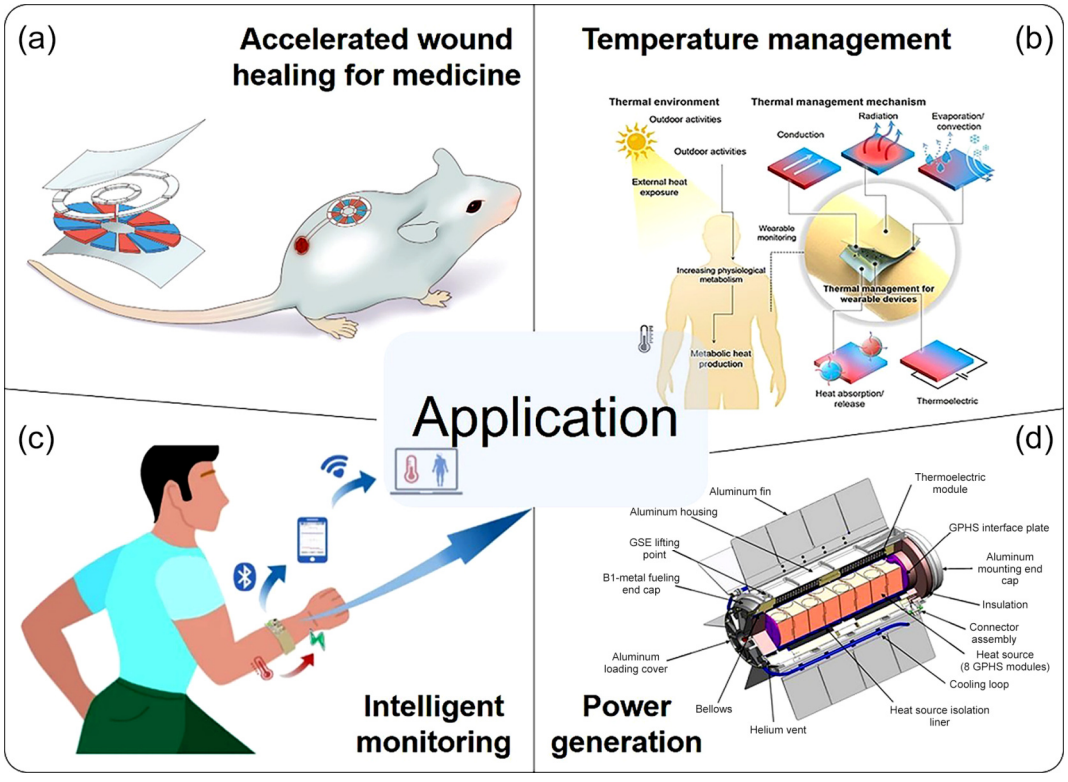

Figure 11 Potential application scenarios for porous TE materials. (a) Accelerated wound healing for medicine. Reproduced with permission from Ref. [59], © Wiley-VCH GmbH 2024. (b) Temperature management for wearable TE coolers based on wearable Peltier effect. Reproduced with permission from Ref. [61], © Yun, J. et al. 2023. (c) The wearable TEG for body temperature sensors and Bluetooth communication. Reproduced with permission from Ref. [62], © Yang, S. et al. 2023. (d) The construction in RTGs for aerospace where lightweight TEG is necessary. Reproduced with permission from Ref. [63], © Zoui, M. A. et al. 2020.

normothermia and promote wound healing. By integrating thermoelectric materials with conductive textiles, the system ensures efficient heat distribution while minimizing power consumption through a pulse-width modulation control mechanism. The findings provide another route for the design and development of porous thermoelectric devices for wound care and management [175].

5.2.2 *Temperature management*

TE coolers based on Peltier effect are gaining interest as replacements for traditional cooling and refrigeration systems. Wearable semiconductor cooling pads designed for localized cooling of the human body could reduce reliance on traditional environmental cooling methods, such as air conditioners and compressors, mitigate global warming and lower energy costs (Fig. 11(b)). Due to the inferior heat exchange efficiency between human skin and ambient air, wearable TE cooling pads face significant thermal resistance. This external thermal resistance greatly impacts the behavior of TE materials, influencing both the design and performance of the device. Overcoming this challenge is critical for achieving high efficiency in body-sensing applications, as it affects the overall cooling effectiveness and energy efficiency of wearable TE systems. Optimized designs must account for these resistances to improve the device's thermal management and functionality. Kishore et al. explored the combined impact of thermal resistances at heat sources/sinks and TE material properties on the performance of TE coolers [145]. Their findings demonstrated that optimized coolers could lower skin temperature by up to 8.2 °C below ambient levels, delivering 170% more cooling than commercial modules. Additionally, a cost-benefit analysis revealed that cooling efficiency per unit volume for these optimized coolers is 500% greater than that of commercial counterparts, highlighting their superior performance and economic advantages in wearable applications. Furthermore, Gao et al. developed a wearable personal thermoelectric cooler (WTEC) featuring a honeycomb-structured encapsulation and low thermal conductivity filler, enabling enhanced flexibility, mechanical resilience, and thermal insulation [176]. By incorporating SiO_2 aerogel, hollow glass beads, and PDMS, the design minimizes heat leakage while maintaining structural integrity. A hexagonal boron nitride (HBN)-based radiative cooling film further optimizes heat dissipation. The device achieves a cooling temperature difference of 9.1 °C indoors and 6.5 °C outdoors, demonstrating high efficiency in personal thermal management. Finite element analysis (FEA) confirms its superior adaptability and performance, positioning honeycomb wearable thermoelectric cooler as a promising innovation for wearable electronics, smart textiles, and next-generation thermal regulation technologies.

5.2.3 *Intelligent monitoring*

Wearable devices hold the potential to transform human–machine interactions, but their widespread application faces a significant hurdle in the need for continuous, efficient power supply. These devices rely on stable energy sources to handle data-heavy sensing and transmission, adding complexity to their design (Fig. 11(c)). Traditional TE solutions are inadequate in low-voltage conditions. To address this, Yang et al. developed a novel wearable TE generator with an integrated energy management system [62]. This system efficiently converts body heat into energy for sensors and Bluetooth communication, even when the temperature difference

between skin and the environment is as low as 4 K. The system can transmit data reliably within 1.6 s and, crucially, charges using body heat at voltages as low as 30 mV.

Gao et al. presented a self-powered, resilient porous sensor by integrating thermoelectric PEDOT:polystyrenesulfonic acid (PSS) and carbon nanotubes onto a melamine sponge for dual-mode temperature and pressure sensing [177]. The sensor independently detects temperature gradients (Seebeck effect, 35.9 $\mu V \cdot K^{-1}$) and pressure variations (piezoresistive effect, −3.35 $\%\cdot kPa^{-1}$, 4 Pa limit). Its lightweight, flexible, and porous structure ensures durability and high sensitivity, making it ideal for wearable electronics, artificial skin, and biomedical applications. Additionally, it demonstrates self-powered operation under illumination, enhancing its potential for sustainable energy and smart sensing systems.

Interestingly, Yang et al. found a self-powered, stretchable thermoelectric sensor based on porous laser-induced graphene (LIG) foam, designed for simultaneous and decoupled strain–temperature sensing. Fabricated via a low-cost laser scribing process, the sensor leverages the synergistic effect between porous graphene and thermoelectric PEDOT:PSS, achieving a Seebeck coefficient enhancement of nearly fourfold (9.703 to 37.33 $\mu V \cdot °C^{-1}$) [178]. It demonstrates high strain sensitivity (gauge factor of 1401.5) and a temperature resolution of 0.5 °C, ensuring precise, interference-free detection. The system enables real-time wound healing monitoring, highlighting its potential for wearable electronics, biomedical applications, and remote sensing systems. More importantly, if such temperature monitoring and accelerated wound healing techniques are combined based on the thermoelectric effect jointly, the multifunctional devices for sensor-treatment integration could potentially be developed.

These breakthroughs offer a new approach to powering standalone wearable devices, enabling continuous monitoring without the need for batteries. By ensuring reliable energy conversion and transmission, this development could pave the way for widespread, practical adoption of wearable technologies across various sectors, including healthcare and fitness.

5.2.4 Power generation

RTG is a device that converts the heat released by radioactive decay into electrical energy. It operates based on the TE effect, where a temperature difference across TE materials generates an electric current. Figure 11(d) shows the construction for RTGs where the heat from radioactive isotopes such as plutonium-238 creates a temperature gradient across the TE materials, resulting in electrical power. RTGs are crucial for aerospace craft, where solar power is insufficient due to the far away distance from the sun. The RTGs provide a reliable and long-lasting power source for spacecraft, enabling them to perform extended missions and support scientific instruments and communication systems. PbTe is a commonly used TE material in RTGs, but with a high density of 8 $g \cdot cm^{-3}$, which is an order of magnitude heavier than the average density of spacecraft (0.5 $g \cdot cm^{-3}$). The TE microlattices fabricated using direct ink writing technology display a high specific energy absorption 28 $J \cdot g^{-1}$ much higher than that of typical TE semiconductors BiSbTe (0.5 $J \cdot g^{-1}$), InSe (4 $J \cdot g^{-1}$), Ag_2S (6 $J \cdot g^{-1}$), and $AgTe_{0.6}S_{0.4}$ (6 $J \cdot g^{-1}$) [137]. This optimization increases the payload capacity and propulsion limits of the spacecraft, making RTGs critical for long-duration space exploration. In addition, porous TEGs have also made a difference in daily life. For example, A lightweight, flexible porous Ag_2Se film-based TEGs for near-room-temperature energy harvesting. Using a scalable screen printing and annealing process, freestanding Ag_2Se films with tunable pore densities achieve a balance between mechanical flexibility and thermoelectric performance. High-density porous films enhance flexibility, while low-density porous films reach a power factor of 1240 $\mu W \cdot m^{-1} \cdot K^{-2}$ at 300 K. Integrating a PDMS skeleton improves stability, retaining 96% conductivity after 1000 bending cycles. A five-leg TEG generates 20.2 mV and 810 nW at a 30 K of temperature difference, demonstrating lightweight durability for wearable and energy-harvesting applications [46].

Despite the incorporation of porosity into materials to impart additional properties such as lightweight and deformability, significant challenges may arise in practical applications. On the one hand, the presence of pores substantially affects the electrical performance. While some studies have suggested that appropriately designed porosity can decouple thermoelectric parameters, most high-performance thermoelectric materials are still given by dense materials [179–181]. This is probably due to the narrow threshold of the optimal parameters of the pores, which otherwise cannot compensate for the lost electrical properties. Consequently, the complex synthesis methods for porous thermoelectric materials require to control precisely. On the other hand, the long-term service performance of porous thermoelectric materials is crucial. Extended operation may result in material fatigue or chemical reaction due to the loosen structures with pores, which may lead to performance degradation. Therefore, the development of efficient porous thermoelectric devices and his stability verification is still a topic that needs to be continued research.

6 Conclusion and outlook

6.1 Conclusion

This paper provides a comprehensive review of the recent advances in the development of porous thermoelectric materials, focusing on the diverse preparation methods, classification of pore structures, and their effects on TE performance. The introduction of pores has been demonstrated as an effective strategy for significantly reducing κ_L, which in turn enhances TE efficiency. Representative synthesis techniques, such as sintering process optimization, freeze-drying, direct ink writing, and chemical etching, have been systematically examined, showing their effect in creating controlled porous structures. While porous structures improve thermal insulation, they can also degrade electrical conductivity due to increased phonon scattering. To address this, strategies such as doping, defect incorporation, and the combination of nanostructures with porous designs have been explored to maintain a balance between electrical and thermal properties. Additionally, the review discussed the design principles for TE devices that incorporate porous materials to achieve high efficiency, flexibility, conformability, and lightweight systems for applications in areas such as aerospace, wearable electronics, and energy harvesting.

Porous TE materials show great potential in applications requiring high-temperature stability, reduced material costs, and optimized TE performance. The lower density achieved through the introduction of pores not only reduces material weight but also contributes to improved mechanical, particularly in high-temperature applications. These characteristics make porous TE materials promising candidates for future applications in aviation, military equipment, and medical devices.

6.2 Outlook

Moving forward, several critical research directions need to be explored to further enhance the performance and applicability of porous TE materials. The design and control of pore structures will play a key role in overcoming current limitations and unlocking new potentials:

6.2.1 *Optimization of pore design*

The design of pore structures should consider both TE performance and flexibility. TE performance is enhanced by optimizing pore structures to decouple electrical and thermal properties—reducing κ_L through phonon scattering while maintaining electrical conductivity. Flexibility can be improved through various design strategies, such as fractal-inspired structures, which allow the material to remain flexible under deformation while ensuring TE efficiency. Artificial intelligence (AI) may further play a supportive role in the design and development of these porous structures by aiding in the precise control of pore distribution, size, and geometry. By carefully combining traditional design methods with AI assistance, a balance can be achieved between TE performance and mechanical flexibility.

6.2.2 *Compensation of electrical conductivity*

The challenge of maintaining or enhancing electrical conductivity in porous materials remains crucial. One approach is to integrate conductive networks within the porous matrix, such as using nanowires, carbon nanotubes, or conductive polymers. These networks can facilitate charge transport while the porous structure suppresses κ_L. The combination of such conductive frameworks with pore design can optimize the ZT, allowing it to perform well even under high-temperature conditions. Additionally, band engineering and energy filtering strategies could be employed to mitigate the adverse effects of pore-induced scattering on carrier mobility.

6.2.3 *Scalable fabrication techniques*

For porous TE materials to transition from laboratory-scale experiments to commercial applications, scalable and cost-effective fabrication methods need to be developed. Current techniques like spark plasma sintering, freeze-drying, and chemical etching, while effective, present challenges for large-scale production. Emerging methods such as 3D printing and direct ink writing show great promise for creating complex and high-performance porous structures on a larger scale. These techniques provide precise control over pore geometry and distribution, enabling the design of more efficient TE materials that can be manufactured at lower costs. Note that the AI design pore configuration is thought to accomplish functional diversity. Combining with AI-designed, more diverse structures and properties can be manufactured by advanced 3D printing and direct ink writing techniques in microscale.

6.2.4 *Development of flexible and conformable devices*

The future of TE technology lies in flexible and conformable devices, particularly for wearable electronics and soft mechanical components. To meet these needs, researchers should explore novel materials that combine high TE performance with mechanical flexibility. Materials with tunable pore structures that can endure mechanical deformations, such as bending, stretching, and twisting, without a significant loss in efficiency, are particularly valuable. The use of composite materials, including polymers or elastomers infused with TE nanoparticles, could be a promising direction. These materials can maintain electrical conductivity even when stretched or compressed, making them ideal for wearable TE generators (TEGs) and other flexible energy-harvesting devices.

6.2.5 *Integration into multifunctional systems*

Porous TE materials have the potential to be integrated into multifunctional systems that go beyond simple energy conversion. For example, TE materials could be combined with sensors to create self-powered devices capable of monitoring environmental conditions, health metrics, or industrial processes. These devices could harvest waste heat from their surroundings, making them ideal for remote or inaccessible locations. Future research could focus on integrating TE materials with other functional materials, such as catalysts or energy storage components, to develop smart systems that offer both power generation and additional functionalities.

Data availability

Not applicable.

Acknowledgements

C. J. Z. acknowledges the National Natural Science Foundation of China (No. 22379124), the National Science Fund for Excellent Young Scientist Fund Program (Overseas) of China, Research Fund of the State Key Laboratory of Solidification Processing (NPU) (No. China 2023-QZ-01), and the Fund for State Key Laboratory (No. 6142806230202). B. Z. G. thanks the support from China Postdoctoral Science Foundation(Certificate No. 2024M764249) and the Research Fund of the State Key Laboratory of Solidification Processing (NPU), China (No. 2024-BJ-01).

Declaration of competing interest

All the contributing authors report no conflict of interests in this work.

Author contribution statement

B. Z. G. and C. J. Z. conceived, designed, and supervised the entire project. R. Y. L. collected the data, conducted the figures, and wrote the first draft. B. Z. G. revised the manuscript with inputs from all authors. All the authors have approved the final manuscript.

Informed consent

Not applicable.

Ethics statement

Not applicable.

Use of AI statement

None.

References

[1] Liu, M.; Guo, M. C.; Lyu, H.; Lai, Y. D.; Zhu, Y. K.; Guo, F. K.; Yang, Y. Y.; Yu, K.; Dong, X. Y.; Liu, Z. H. et al. Doping strategy

in metavalently bonded materials for advancing thermoelectric performance. *Nat. Commun.* **2024**, *15*, 8286.
[2] Qin, B. C.; Kanatzidis, M. G.; Zhao, L. D. The development and impact of tin selenide on thermoelectrics. *Science* **2024**, *386*, eadp2444.
[3] Zhu, Y. K.; Sun, Y. X.; Dong, X. Y.; Yin, L.; Liu, M.; Guo, M. C.; Wu, H.; Li, F. S.; Guo, Z. T.; Wang, X. Y. et al. General design of high-performance and textured layered thermoelectric materials via stacking of mechanically exfoliated crystals. *Joule* **2024**, *8*, 2412–2424.
[4] Bhui, A.; Biswas, K. Mobile ion confinement for better thermoelectrics. *Nat. Mater.* **2024**, *23*, 451–452.
[5] Jiang, B. B.; Wang, W.; Liu, S. X.; Wang, Y.; Wang, C. F.; Chen, Y. N.; Xie, L.; Huang, M. Y.; He, J. Q. High figure-of-merit and power generation in high-entropy GeTe-based thermoelectrics. *Science* **2022**, *377*, 208–213.
[6] Chen, Y. X.; Shi, X. L.; Zhang, J. Z.; Nisar, M.; Zha, Z. Z.; Zhong, Z. N.; Li, F.; Liang, G. X.; Luo, J. T.; Li, M. et al. Deviceization of high-performance and flexible Ag_2Se films for electronic skin and servo rotation angle control. *Nat. Commun.* **2024**, *15*, 8356.
[7] Qin, Y. X.; Qin, B. C.; Hong, T.; Zhang, X.; Wang, D. Y.; Liu, D. R.; Wang, Z. Y.; Su, L. Z.; Wang, S. N.; Gao, X. et al. Grid-plainification enables medium-temperature PbSe thermoelectrics to cool better than Bi_2Te_3. *Science* **2024**, *383*, 1204–1209.
[8] Xie, L. J.; Yin, L.; Yu, Y.; Peng, G. Y.; Song, S. W.; Ying, P. J.; Cai, S. T.; Sun, Y. X.; Shi, W. J.; Wu, H. et al. Screening strategy for developing thermoelectric interface materials. *Science* **2023**, *382*, 921–928.
[9] Ming, H. W.; Luo, Z. Z.; Chen, Z. X.; Cui, H. H.; Zheng, W. W.; Zou, Z. G.; Kanatzidis, M. G. Chemical pressure-driven band convergence and discordant atoms intensify phonon scattering leading to high thermoelectric performance in SnTe. *J. Am. Chem. Soc.* **2024**, *146*, 28448–28458.
[10] Ghosh, S.; Nozariasbmarz, A.; Lee, H.; Raman, L.; Sharma, S.; Smriti, R. B.; Mandal, D.; Zhang, Y.; Karan, S. K.; Liu, N. et al. High-entropy-driven half-Heusler alloys boost thermoelectric performance. *Joule* **2024**, *8*, 3303–3312.
[11] Mao, D. S.; Zhou, Y.; Yu, Y.; Wang, Y.; Han, M.; Meng, Q. Y.; Lu, Y.; Feng, J. H.; Kong, M. H.; Yang, H. L. et al. Scalable and sustainable manufacturing of twin boundary-enhanced flexible $Bi_{0.4}Sb_{1.6}Te_3$ films with high thermoelectric performance. *Joule* **2024**, *8*, 3313–3323.
[12] Shi, X.; Song, S. W.; Gao, G. H.; Ren, Z. F. Global band convergence design for high-performance thermoelectric power generation in Zintls. *Science* **2024**, *384*, 757–762.
[13] Zhao, P.; Xue, W. H.; Zhang, Y.; Zhi, S. Z.; Ma, X. J.; Qiu, J. M.; Zhang, T. Y.; Ye, S.; Mu, H. M.; Cheng, J. X. et al. Plasticity in single-crystalline Mg_3Bi_2 thermoelectric material. *Nature* **2024**, *631*, 777–782.
[14] Liu, M.; Zhang, X. Y.; Zhang, S. X.; Pei, Y. Z. Ag_2Se as a tougher alternative to n-type Bi_2Te_3 thermoelectrics. *Nat. Commun.* **2024**, *15*, 6580.
[15] Yu, H. L.; Hu, Z. Q.; He, J.; Ran, Y. J.; Zhao, Y.; Yu, Z.; Tai, K. P. Flexible temperature-pressure dual sensor based on 3D spiral thermoelectric Bi_2Te_3 films. *Nat. Commun.* **2024**, *15*, 2521.
[16] Cheng, R.; Ge, H. R.; Huang, S. P.; Xie, S.; Tong, Q. W.; Sang, H.; Yan, F.; Zhu, L. Y.; Wang, R.; Liu, Y. et al. Unraveling electronic origins for boosting thermoelectric performance of p-type $(Bi, Sb)_2Te_3$. *Sci. Adv.* **2024**, *10*, eadn9959.
[17] An, D. C.; Zhang, S. H.; Zhai, X.; Yang, W. T.; Wu, R. G.; Zhang, H. D.; Fan, W. H.; Wang, W. X.; Chen, S. P.; Cojocaru-Mirédin, O. et al. Metavalently bonded tellurides: The essence of improved thermoelectric performance in elemental Te. *Nat. Commun.* **2024**, *15*, 3177.
[18] Wu, R. G.; Yu, Y.; Jia, S.; Zhou, C. J.; Cojocaru-Mirédin, O.; Wuttig, M. Strong charge carrier scattering at grain boundaries of PbTe caused by the collapse of metavalent bonding. *Nat. Commun.* **2023**, *14*, 719.
[19] Jia, B. H.; Wu, D.; Xie, L.; Wang, W.; Yu, T.; Li, S. Y.; Wang, Y.; Xu, Y. J.; Jiang, B. B.; Chen, Z. Q. et al. Pseudo-nanostructure and trapped-hole release induce high thermoelectric performance in PbTe. *Science* **2024**, *384*, 81–86.
[20] Fujimoto, S.; Nagase, K.; Ohshima, H.; Murata, M.; Yamamoto, A.; Lee, C. H. Thermoelectric module of SiGe bulk alloys forming p–n junction at the hot side. *Adv. Eng. Mater.* **2022**, *24*, 2101520.
[21] Toko, K.; Maeda, S.; Ishiyama, T.; Nozawa, K.; Murata, M.; Suemasu, T. Layer exchange synthesis of SiGe for flexible thermoelectric generators: A comprehensive review. *Adv. Electron. Mater.* **2024**, *10*, 2400130.
[22] Koike, S.; Yanagisawa, R.; Jalabert, L.; Anufriev, R.; Kurosawa, M.; Mori, T.; Nomura, M. Planar-type SiGe thermoelectric generator with double cavity structure. *Appl. Phys. Lett.* **2024**, *124*, 123902.
[23] Li, A. R.; Wang, Y. C.; Li, Y. Z.; Yang, X. L.; Nan, P. F.; Liu, K.; Ge, B. H.; Fu, C. G.; Zhu, T. J. High performance magnesium-based plastic semiconductors for flexible thermoelectrics. *Nat. Commun.* **2024**, *15*, 5108.
[24] Li, D.; Shi, X. L.; Zhu, J. X.; Cao, T. Y.; Ma, X.; Li, M.; Han, Z. K.; Feng, Z. Y.; Chen, Y. X.; Wang, J. Y. et al. High-performance flexible p-type Ce-filled Fe_3CoSb_{12} skutterudite thin film for medium-to-high-temperature applications. *Nat. Commun.* **2024**, *15*, 4242.
[25] Yin, L.; Yang, F.; Bao, X.; Xue, W. H.; Du, Z. P.; Wang, X. Y.; Cheng, J. X.; Ji, H. J.; Sui, J.; Liu, X. J. et al. Low-temperature sintering of Ag nanoparticles for high-performance thermoelectric module design. *Nat. Energy* **2023**, *8*, 665–674.
[26] Xu, B.; Tian, Y. J. Breaking a bottleneck for thermoelectric generators. *Science* **2023**, *382*, 882–883.
[27] Su, L. Z.; Wang, D. Y.; Wang, S. N.; Qin, B. C.; Wang, Y. P.; Qin, Y. X.; Jin, Y.; Chang, C.; Zhao, L. D. High thermoelectric performance realized through manipulating layered phonon–electron decoupling. *Science* **2022**, *375*, 1385–1389.
[28] Hu, J. S.; Sun, Y. X.; Shi, W. J.; Wu, H.; Zhu, J. B.; Cheng, J. X.; Jiao, L.; Jiang, X. H.; Xie, L. J.; Qu, N. et al. Realizing ultrahigh conversion efficiency of ≈ 9.0% in $YbCd_2Sb_2/Mg_3Sb_2$ zintl module for thermoelectric power generation. *Adv. Mater.* **2024**, *36*, 2411738.
[29] Zhou, Y.; Liu, X. X.; Jia, B. H.; Ding, T. P.; Mao, D. S.; Wang, T. C.; Ho, G. W.; He, J. Q. Physics-guided co-designing flexible thermoelectrics with techno-economic sustainability for low-grade heat harvesting. *Sci. Adv.* **2023**, *9*, eadf5701.
[30] Palaporn, D.; Tanusilp, S. A.; Sun, Y. F.; Pinitsoontorn, S.; Kurosaki, K. Thermoelectric materials for space explorations. *Mater. Adv.* **2024**, *5*, 5351–5364.
[31] Xie, L.; Ming, C.; Song, Q. F.; Wang, C.; Liao, J. C.; Wang, L.; Zhu, C. X.; Xu, F. F.; Sun, Y. Y.; Bai, S. Q. et al. Lead-free and scalable GeTe-based thermoelectric module with an efficiency of 12%. *Sci. Adv.* **2023**, *9*, eadg7919.
[32] Wang, D. Y.; Ding, J. M.; Ma, Y. Q.; Xu, C. L.; Li, Z. Y.; Zhang, X.; Zhao, Y.; Zhao, Y.; Di, Y. Q.; Liu, L. Y. et al. Multi-heterojunctioned plastics with high thermoelectric figure of merit. *Nature* **2024**, *632*, 528–535.
[33] Yang, Q. Y.; Yang, S. Q.; Qiu, P. F.; Peng, L. M.; Wei, T. R.; Zhang, Z.; Shi, X.; Chen, L. F. Flexible thermoelectrics based on ductile semiconductors. *Science* **2022**, *377*, 854–858.
[34] Yu, L.; Shi, X. L.; Mao, Y. Q.; Liu, W. D.; Ji, Z.; Wei, S. T.; Zhang, Z. P.; Song, W. Y.; Zheng, S. Q.; Chen, Z. G. Simultaneously boosting thermoelectric and mechanical properties of n-type $Mg_3Sb_{1.5}Bi_{0.5}$-based zintls through energy-band and defect engineering. *ACS Nano* **2024**, *18*, 1678–1689.
[35] Zhang, X. F.; Zhu, H. T.; Dong, X. J.; Fan, Z.; Yao, Y.; Chen, N.; Yang, J. W.; Guo, K. W.; Hao, J. Z.; He, L. H. et al. High-performance $MgAgSb/Mg_3(Sb, Bi)_2$-based thermoelectrics with η = 12% at $T \leq 583$ K. *Joule* **2024**, *8*, 3324–3335.
[36] Liu, D. R.; Wang, D. Y.; Hong, T.; Wang, Z. Y.; Wang, Y. P.; Qin, Y. X.; Su, L. Z.; Yang, T. Y.; Gao, X.; Ge, Z. H. et al. Lattice plainification advances highly effective SnSe crystalline thermoelectrics. *Science* **2023**, *380*, 841–846.
[37] Qiu, P. F.; Deng, T. T.; Chen, L. D.; Shi, X. Plastic inorganic thermoelectric materials. *Joule* **2024**, *8*, 622–634.

[38] Sun, Y. X.; Guo, F. K.; Feng, Y.; Li, C.; Zou, Y. C.; Cheng, J. X.; Dong, X. Y.; Wu, H.; Zhang, Q.; Liu, W. S. et al. Performance boost for bismuth telluride thermoelectric generator via barrier layer based on low Young's modulus and particle sliding. *Nat. Commun.* **2023**, *14*, 8085.

[39] Tang, G. D.; Liu, Y. Q.; Yang, X. Y.; Zhang, Y. S.; Nan, P. F.; Ying, P.; Gong, Y. R.; Zhang, X. M.; Ge, B. H.; Lin, N. et al. Interplay between metavalent bonds and dopant orbitals enables the design of SnTe thermoelectrics. *Nat. Commun.* **2024**, *15*, 9133.

[40] Wang, L.; Wen, Y.; Bai, S. L.; Chang, C.; Li, Y. C.; Liu, S.; Liu, D. R.; Wang, S. Q.; Zhao, Z.; Zhan, S. P. et al. Realizing thermoelectric cooling and power generation in n-type $PbS_{0.6}Se_{0.4}$ via lattice plainification and interstitial doping. *Nat. Commun.* **2024**, *15*, 3782.

[41] Yang, H. L.; Jia, B. H.; Xie, L.; Mao, D. S.; Xia, J. C.; Yang, J. M.; Yuan, M. H.; Gan, Q.; Liu, X. S.; Hu, M. Y. et al. Achieving high thermoelectric performance through ultra-low lattice thermal conductivity based on phonon localization. *Joule* **2024**, *8*, 2667–2680.

[42] Zheng, Y. Y.; Han, X.; Yang, J. W.; Jing, Y. Y.; Chen, X. Y.; Li, Q. Q.; Zhang, T.; Li, G. D.; Zhu, H. T.; Zhao, H. Z. et al. Durable, stretchable and washable inorganic-based woven thermoelectric textiles for power generation and solid-state cooling. *Energy Environ. Sci.* **2022**, *15*, 2374–2385.

[43] Yu, J. C.; Liu, X. D.; Hu, H. H.; Jiang, Y. L.; Zhuang, H. L.; Li, H. Z.; Su, B.; Li, J. W.; Han, Z. R.; Wang, Z. Q. et al. Ultralow thermal conductivity and high ZT of Cu_2Se-based thermoelectric materials mediated by TiO_{2-n} nanoclusters. *Joule* **2024**, *8*, 2652–2666.

[44] Liu, Z. H.; Gao, W. H.; Oshima, H.; Nagase, K.; Lee, C. H.; Mori, T. Maximizing the performance of n-type Mg_3Bi_2 based materials for room-temperature power generation and thermoelectric cooling. *Nat. Commun.* **2022**, *13*, 1120.

[45] Yang, D.; Shi, X. L.; Li, M.; Nisar, M.; Mansoor, A.; Chen, S.; Chen, Y. X.; Li, F.; Ma, H. L.; Liang, G. X. et al. Flexible power generators by Ag_2Se thin films with record-high thermoelectric performance. *Nat. Commun.* **2024**, *15*, 923.

[46] Wang, H. Y.; Lin, X. Y.; Han, G.; Zhang, B.; Chen, Y.; Zhang, L.; Lu, X.; Wang, G. Y.; Zhou, X. Y. Flexible porous Ag_2Se films: From freestanding inorganic films to inorganic-network/organic-skeleton thermoelectric generators. *Adv. Funct. Mater.* **2025**, *35*, 2413605.

[47] Hu, H. H.; Zhuang, H. L.; Jiang, Y. L.; Shi, J. L.; Li, J. W.; Cai, B. W.; Han, Z. R.; Pei, J.; Su, B.; Ge, Z. H. et al. Thermoelectric $Cu_{12}Sb_4S_{13}$-based synthetic minerals with a sublimation-derived porous network. *Adv. Mater.* **2021**, *33*, 2103633.

[48] Li, J. H.; Xia, B. L.; Xiao, X.; Huang, Z. F.; Yin, J. Y.; Jiang, Y. W.; Wang, S. L.; Gao, H. Q.; Shi, Q. W.; Xie, Y. N. et al. Stretchable thermoelectric fibers with three-dimensional interconnected porous network for low-grade body heat energy harvesting. *ACS Nano* **2023**, *17*, 19232–19241.

[49] Kim, F.; Yang, S. E.; Ju, H.; Choo, S.; Lee, J.; Kim, G.; Jung, S. H.; Kim, S.; Cha, C.; Kim, K. T. et al. Direct ink writing of three-dimensional thermoelectric microarchitectures. *Nat. Electron.* **2021**, *4*, 579–587.

[50] Chen, J. J.; Xie, H.; Liu, L. Z.; Guan, H.; You, Z. S.; Zou, L. J.; Jin, H. J. Strengthening gold with dispersed nanovoids. *Science* **2024**, *385*, 629–633.

[51] Choo, S.; Ejaz, F.; Ju, H.; Kim, F.; Lee, J.; Yang, S. E.; Kim, G.; Kim, H.; Jo, S.; Baek, S. et al. Cu_2Se-based thermoelectric cellular architectures for efficient and durable power generation. *Nat. Commun.* **2021**, *12*, 3550.

[52] Guo, Y.; Mu, J. K.; Hou, C. Y.; Wang, H. Z.; Zhang, Q. H.; Li, Y. G. Flexible and thermostable thermoelectric devices based on large-area and porous all-graphene films. *Carbon* **2016**, *107*, 146–153.

[53] Han, J. K.; Du, G. L.; Gao, W. W.; Bai, H. An anisotropically high thermal conductive boron nitride/epoxy composite based on nacre-mimetic 3D network. *Adv. Funct. Mater.* **2019**, *29*, 1900412.

[54] Tang, J. Y.; Wang, H. T.; Lee, D. H.; Fardy, M.; Huo, Z. Y.; Russell, T. P.; Yang, P. D. Holey silicon as an efficient thermoelectric material. *Nano Lett.* **2010**, *10*, 4279–4283.

[55] Zhang, T.; Wu, S. L.; Xu, J.; Zheng, R. T.; Cheng, G. A. High thermoelectric figure-of-merits from large-area porous silicon nanowire arrays. *Nano Energy* **2015**, *13*, 433–441.

[56] Qian, X.; Zhou, J. W.; Chen, G. Phonon-engineered extreme thermal conductivity materials. *Nat. Mater.* **2021**, *20*, 1188–1202.

[57] He, J.; Tritt, T. M. Advances in thermoelectric materials research: Looking back and moving forward. *Science* **2017**, *357*, eaak9997.

[58] Ryu, B.; Chung, J.; Kumagai, M.; Mato, T.; Ando, Y.; Gunji, S.; Tanaka, A.; Yana, D.; Fujimoto, M.; Imai, Y. et al. Best thermoelectric efficiency of ever-explored materials. *iScience* **2023**, *26*, 106494.

[59] Zhang, Y. W.; Ge, B. Z.; Feng, J. H.; Kuang, N. L.; Ye, H. L.; Yuan, Z. L.; Wu, M. Y.; Jiang, B. B.; Li, J.; Sun, Q. et al. High-performance self-powered flexible thermoelectric device for accelerated wound healing. *Adv. Funct. Mater.* **2024**, *34*, 2403990.

[60] Fan, J. A.; Yeo, W. H.; Su, Y. W.; Hattori, Y.; Lee, W.; Jung, S. Y.; Zhang, Y. H.; Liu, Z. J.; Cheng, H. Y.; Falgout, L. et al. Fractal design concepts for stretchable electronics. *Nat. Commun.* **2014**, *5*, 3266.

[61] Yun, J.; Yoo, Y. J.; Kim, H. R.; Song, Y. M. Recent progress in thermal management for flexible/wearable devices. *Soft Sci.* **2023**, *3*, 12.

[62] Yang, S.; Li, Y. M.; Deng, L.; Tian, S.; Yao, Y.; Yang, F.; Feng, C. L.; Dai, J.; Wang, P.; Gao, M. Y. Flexible thermoelectric generator and energy management electronics powered by body heat. *Microsyst. Nanoeng.* **2023**, *9*, 106.

[63] Zoui, M. A.; Bentouba, S.; Stocholm, J. G.; Bourouis, M. A review on thermoelectric generators: Progress and applications. *Energies* **2020**, *13*, 3606.

[64] Yousefi, E.; Abbas Nejad, A.; Sayyar, N. A new approach for simultaneous thermal management of hot and cold sides of thermoelectric modules. *Appl. Therm. Eng.* **2023**, *233*, 121156.

[65] Al-Madhhachi, H.; Min, G. Effective use of thermal energy at both hot and cold side of thermoelectric module for developing efficient thermoelectric water distillation system. *Energy Convers. Manage.* **2017**, *133*, 14–19.

[66] Wang, D. Z.; Liu, W. D.; Mao, Y. Q.; Li, S.; Yin, L. C.; Wu, H.; Li, M.; Wang, Y. F.; Shi, X. L.; Yang, X. N. et al. Decoupling carrier-phonon scattering boosts the thermoelectric performance of n-type GeTe-based materials. *J. Am. Chem. Soc.* **2024**, *146*, 1681–1689.

[67] Si, R. F.; Zhang, Z. W.; Liu, C. Y.; Peng, Y.; Bai, X. B.; Feng, B. Q.; Chen, J. L.; Gao, J.; Miao, L. Decoupled electron and phonon transport in thermoelectric GeTe compounded with multi-walled carbon nanotubes. *Mater. Today Phys.* **2023**, *34*, 101081.

[68] Jin, K. P.; Tiwari, J.; Feng, T. L.; Lou, Y.; Xu, B. Realizing high thermoelectric performance in eco-friendly Bi_2S_3 with nanopores and Cl-doping through shape-controlled nano precursors. *Nano Energy* **2022**, *100*, 107478.

[69] Zhang, Y. C.; Day, T.; Snedaker, M. L.; Wang, H.; Krämer, S.; Birkel, C. S.; Ji, X. L.; Liu, D. Y.; Snyder, G. J.; Stucky, G. D. A mesoporous anisotropic n-type Bi_2Te_3 monolith with low thermal conductivity as an efficient thermoelectric material. *Adv. Mater.* **2012**, *24*, 5065–5070.

[70] Ning, H. P.; Mastrorillo, G. D.; Grasso, S.; Du, B. L.; Mori, T.; Hu, C. F.; Xu, Y.; Simpson, K.; Maizza, G.; Reece, M. J. Enhanced thermoelectric performance of porous magnesium tin silicide prepared using pressure-less spark plasma sintering. *J. Mater. Chem. A* **2015**, *3*, 17426–17432.

[71] Wu, H. J.; Chen, L. L.; Ning, S. T.; Zhao, X. D.; Deng, S. P.; Qi, N.; Ren, F.; Chen, Z. Q.; Tang, J. Extremely low thermal conductivity and enhanced thermoelectric performance of porous gallium-doped In_2O_3. *ACS Appl. Energy Mater.* **2021**, *4*, 12943–12953.

[72] Chen, J.; Sun, Q.; Bao, D. Y.; Liu, T. Y.; Liu, W. D.; Liu, C.; Tang, J.; Zhou, D. L.; Yang, L.; Chen, Z. G. Hierarchical structures advance thermoelectric properties of porous n-type β-Ag_2Se. *ACS Appl. Mater. Interfaces* **2020**, *12*, 51523–51529.

[73] Lee, M. H.; Kang, Y. H.; Kim, J.; Lee, Y. K.; Cho, S. Y. Freely shapable and 3D porous carbon nanotube foam using rapid solvent

evaporation method for flexible thermoelectric power generators. *Adv. Energy Mater.* **2019**, *9*, 1900914.
[74] Okada, N.; Sato, K.; Yokoo, M.; Kodama, E.; Kanehashi, S.; Shimomura, T. Thermoelectric properties of poly(3-hexylthiophene) nanofiber aerogels with a giant Seebeck coefficient. *ACS Appl. Polym. Mater.* **2021**, *3*, 455–463.
[75] Gnanaseelan, M.; Chen, Y. A.; Luo, J. J.; Krause, B.; Pionteck, J.; Pötschke, P.; Qi, H. S. Cellulose-carbon nanotube composite aerogels as novel thermoelectric materials. *Compos. Sci. Technol.* **2018**, *163*, 133–140.
[76] Gordon, M. P.; Zaia, E. W.; Zhou, P.; Russ, B.; Coates, N. E.; Sahu, A.; Urban, J. J. Soft PEDOT: PSS aerogel architectures for thermoelectric applications. *J. Appl. Polym. Sci.* **2017**, *134*, 44070.
[77] Wang, X. D.; Liang, L. R.; Lv, H. C.; Zhang, Y. C.; Chen, G. M. Elastic aerogel thermoelectric generator with vertical temperature-difference architecture and compression-induced power enhancement. *Nano Energy* **2021**, *90*, 106577.
[78] Tan, D. X.; Zhao, J.; Gao, C. Y.; Wang, H. F.; Chen, G. M.; Shi, D. L. Carbon nanoparticle hybrid aerogels: 3D double-interconnected network porous microstructure, thermoelectric, and solvent-removal functions. *ACS Appl. Mater. Interfaces* **2017**, *9*, 21820–21828.
[79] Hull, C. W. Apparatus for production of three-dimensional objects by stereolithography. U.S. Patent 4,575,330, March 11, 1986.
[80] Kim, F.; Kwon, B.; Eom, Y.; Lee, J. E.; Park, S.; Jo, S.; Park, S. H.; Kim, B. S.; Im, H. J.; Lee, M. H. et al. 3D printing of shape-conformable thermoelectric materials using all-inorganic Bi_2Te_3-based inks. *Nat. Energy* **2018**, *3*, 301–309.
[81] Choo, S.; Lee, J.; Şişik, B.; Jung, S. J.; Kim, K.; Yang, S. E.; Jo, S.; Nam, C.; Ahn, S.; Lee, H. S. et al. Geometric design of Cu_2Se-based thermoelectric materials for enhancing power generation. *Nat. Energy* **2024**, *8*, 1105–1116.
[82] Zhang, D. W.; Lim, X. J. G.; Li, X. W.; Saglik, K.; Solco, S. F. D.; Tan, X. Y.; Leow, Y.; Zhai, W.; Tan, C. K. I.; Xu, J. W. et al. 3D-printed porous thermoelectrics for *in situ* energy harvesting. *ACS Energy Lett.* **2023**, *8*, 332–338.
[83] Qiu, J. H.; Yan, Y. G.; Luo, T. T.; Tang, K. C.; Yao, L.; Zhang, J.; Zhang, M.; Su, X. L.; Tan, G. J.; Xie, H. Y. et al. 3D Printing of highly textured bulk thermoelectric materials: Mechanically robust BiSbTe alloys with superior performance. *Energy Environ. Sci.* **2019**, *12*, 3106–3117.
[84] Zhang, Y. H.; Xu, G. Y.; Han, F.; Wang, Z.; Ge, C. C. Preparation and thermoelectric properties of nanoporous Bi_2Te_3-based alloys. *J. Electron. Mater.* **2010**, *39*, 1741–1745.
[85] Wu, C. F.; Wei, T. R.; Sun, F. H.; Li, J. F. Nanoporous PbSe–SiO_2 thermoelectric composites. *Adv. Sci.* **2017**, *4*, 1700199.
[86] Qiao, J. X.; Zhao, Y.; Jin, Q.; Tan, J.; Kang, S. Q.; Qiu, J. H.; Tai, K. P. Tailoring nanoporous structures in Bi_2Te_3 thin films for improved thermoelectric performance. *ACS Appl. Mater. Interfaces* **2019**, *11*, 38075–38083.
[87] Zhao, L. D.; Zhang, B. P.; Liu, W. S.; Zhang, H. L.; Li, J. F. Effects of annealing on electrical properties of n-type Bi_2Te_3 fabricated by mechanical alloying and spark plasma sintering. *J. Alloys Compd.* **2009**, *467*, 91–97.
[88] Schmidt, R. D.; Case, E. D.; Ni, J. E.; Sakamoto, J. S.; Trejo, R. M.; Lara-Curzio, E.; Payzant, E. A.; Kirkham, M. J.; Peascoe-Meisner, R. A. The temperature dependence of thermal expansion for p-type $Ce_{0.9}Fe_{3.5}Co_{0.5}Sb_{12}$ and n-type $Co_{0.95}Pd_{0.05}Te_{0.05}Sb_3$ skutterudite thermoelectric materials. *Philos. Mag.* **2012**, *92*, 1261–1286.
[89] Khan, A. U.; Kobayashi, K.; Tang, D. M.; Yamauchi, Y.; Hasegawa, K.; Mitome, M.; Xue, Y. M.; Jiang, B. Z.; Tsuchiya, K.; Golberg, D. et al. Nano-micro-porous skutterudites with 100% enhancement in ZT for high performance thermoelectricity. *Nano Energy* **2017**, *31*, 152–159.
[90] Morata, A.; Pacios, M.; Gadea, G.; Flox, C.; Cadavid, D.; Cabot, A.; Tarancón, A. Large-area and adaptable electrospun silicon-based thermoelectric nanomaterials with high energy conversion efficiencies. *Nat. Commun.* **2018**, *9*, 4759.
[91] Hochbaum, A. I.; Chen, R. K.; Delgado, R. D.; Liang, W. J.; Garnett, E. C.; Najarian, M.; Majumdar, A.; Yang, P. D. Enhanced thermoelectric performance of rough silicon nanowires. *Nature* **2008**, *451*, 163–167.
[92] de Boor, J.; Kim, D. S.; Ao, X.; Becker, M.; Hinsche, N. F.; Mertig, I.; Zahn, P.; Schmidt, V. Thermoelectric properties of porous silicon. *Appl. Phys. A* **2012**, *107*, 789–794.
[93] Ju, H.; Kim, J. Anion-exchanged porous SnTe nanosheets for ultra-low thermal conductivity and high-performance thermoelectrics. *Chem. Eng. J.* **2020**, *402*, 126274.
[94] Ju, H.; Kim, K.; Park, D.; Kim, J. Fabrication of porous SnSeS nanosheets with controlled porosity and their enhanced thermoelectric performance. *Chem. Eng. J.* **2018**, *335*, 560–566.
[95] Zhao, K. P.; Duan, H. Z.; Raghavendra, N.; Qiu, P. F.; Zeng, Y.; Zhang, W. Q.; Yang, J. H.; Shi, X.; Chen, L. D. Solid-state explosive reaction for nanoporous bulk thermoelectric materials. *Adv. Mater.* **2017**, *29*, 1701148.
[96] Pan, Y.; Aydemir, U.; Grovogui, J. A.; Witting, I. T.; Hanus, R.; Xu, Y. B.; Wu, J. S.; Wu, C. F.; Sun, F. H.; Zhuang, H. L. et al. Melt-centrifuged $(Bi, Sb)_2Te_3$: Engineering microstructure toward high thermoelectric efficiency. *Adv. Mater.* **2018**, *30*, 1802016.
[97] Dun, C.; Hewitt, C. A.; Jiang, Q. K.; Guo, Y.; Xu, J. W.; Li, Y.; Li, Q.; Wang, H. Z.; Carroll, D. L. Bi_2Te_3 plates with single nanopore: The formation of surface defects and self-repair growth. *Chem. Mater.* **2018**, *30*, 1965–1970.
[98] Xu, B.; Feng, T. L.; Li, Z.; Pantelides, S. T.; Wu, Y. Constructing highly porous thermoelectric monoliths with high-performance and improved portability from solution-synthesized shape-controlled nanocrystals. *Nano Lett.* **2018**, *18*, 4034–4039.
[99] Xu, B.; Feng, T. L.; Agne, M. T.; Zhou, L.; Ruan, X. L.; Snyder, G. J.; Wu, Y. Highly porous thermoelectric nanocomposites with low thermal conductivity and high figure of merit from large-scale solution-synthesized $Bi_2Te_{2.5}Se_{0.5}$ hollow nanostructures. *Angew. Chem., Int. Ed.* **2017**, *56*, 3546–3551.
[100] Hu, L. P.; Wu, H. J.; Zhu, T. J.; Fu, C. G.; He, J. Q.; Ying, P. J.; Zhao, X. B. Tuning multiscale microstructures to enhance thermoelectric performance of n-type bismuth-telluride-based solid solutions. *Adv. Energy Mater.* **2015**, *5*, 1500411.
[101] Pan, Y.; Li, J. F. Thermoelectric performance enhancement in *n*-type $Bi_2(TeSe)_3$ alloys owing to nanoscale inhomogeneity combined with a spark plasma-textured microstructure. *NPG Asia Mater.* **2016**, *8*, e275–e275.
[102] Hong, M.; Chasapis, T. C.; Chen, Z. G.; Yang, L.; Kanatzidis, M. G.; Snyder, G. J.; Zou, J. n-Type $Bi_2Te_{3-x}Se_x$ nanoplates with enhanced thermoelectric efficiency driven by wide-frequency phonon scatterings and synergistic carrier scatterings. *ACS Nano* **2016**, *10*, 4719–4727.
[103] Romano, G.; Grossman, J. C. Toward phonon-boundary engineering in nanoporous materials. *Appl. Phys. Lett.* **2014**, *105*, 033116.
[104] Zhang, J.; Zhu, T.; Zhang, C.; Yan, Y. G.; Tan, G. J.; Liu, W.; Su, X. L.; Tang, X. F. *In-situ* formed nano-pore induced by Ultrasonication boosts the thermoelectric performance of Cu_2Se compounds. *J. Alloys Compd.* **2021**, *881*, 160639.
[105] Zhang, W.; Al-Maythalony, B. A.; Gao, F.; Wu, F.; Zhao, W.; Xu, P.; Zhang, W.; Chen, C.; Shi, Z.; Wang, X. et al. Thermally stable inorganic $Bi_{0.4}Sb_{1.6}Te_3$/metal–organic framework (MOF) composites with 1-by-1 nm pore engineering towards mid-temperature thermoelectrics. *Energy Environ. Sci.* **2024**, *17*, 5679–5690.
[106] Slack, G. A. The thermal conductivity of nonmetallic crystals. *Solid State Phys.* **1979**, *34*, 1–71.
[107] Li, S. K.; Wang, R.; Zhu, W. M.; Chu, M. H.; Huang, Z. Y.; Zhang, Y. J.; Zhao, W. G.; Liu, F. S.; Luo, J.; Xiao, Y. G. et al. Achieving high thermoelectric performance by introducing 3D atomically thin conductive framework in porous $Bi_2Te_{2.7}Se_{0.3}$-carbon nanotube hybrids. *Adv. Electron. Mater.* **2020**, *6*, 2000292.
[108] Zen, N.; Puurtinen, T. A.; Isotalo, T. J.; Chaudhuri, S.; Maasilta, I. J. Engineering thermal conductance using a two-dimensional phononic crystal. *Nat. Commun.* **2014**, *5*, 3435.
[109] Li, Y.; Li, W.; Han, T. C.; Zheng, X.; Li, J. X.; Li, B. W.; Fan, S. H.;

Qiu, C. W. Transforming heat transfer with thermal metamaterials and devices. *Nat. Rev. Mater.* **2021**, *6*, 488–507.
[110] Ma, H.; Li, C.; Ma, Y. W.; Wang, H.; Rouse, Z. W.; Zhang, Z. L.; Slebodnick, C.; Alatas, A.; Baker, S. P.; Urban, J. J. et al. Supercompliant and soft $(CH_3NH_3)_3Bi_2I_9$ crystal with ultralow thermal conductivity. *Phys. Rev. Lett.* **2019**, *123*, 155901.
[111] Hofmeister, A. M. Mantle values of thermal conductivity and the geotherm from phonon lifetimes. *Science* **1999**, *283*, 1699–1706.
[112] Kim, D. S.; Hellman, O.; Shulumba, N.; Saunders, C. N.; Lin, J. Y. Y.; Smith, H. L.; Herriman, J. E.; Niedziela, J. L.; Abernathy, D. L.; Li, C. W. et al. Temperature-dependent phonon lifetimes and thermal conductivity of silicon by inelastic neutron scattering and *ab initio* calculations. *Phys. Rev. B* **2020**, *102*, 174311.
[113] Xie, L. J.; Yang, J. W.; Liu, Z. Y.; Qu, N.; Dong, X. Y.; Zhu, J. B.; Shi, W. J.; Wu, H.; Peng, G. Y.; Guo, F. K. et al. Highly efficient thermoelectric cooling performance of ultrafine-grained and nanoporous materials. *Mater. Today* **2023**, *65*, 5–13.
[114] Hong, M.; Wang, Y.; Xu, S. D.; Shi, X.; Chen, L. D.; Zou, J.; Chen, Z. G. Nanoscale pores plus precipitates rendering high-performance thermoelectric $SnTe_{1-x}Se_x$ with refined band structures. *Nano Energy* **2019**, *60*, 1–7.
[115] Shi, X. L.; Wu, A. Y.; Liu, W. D.; Moshwan, R.; Wang, Y.; Chen, Z. G.; Zou, J. Polycrystalline SnSe with extraordinary thermoelectric property via nanoporous design. *ACS Nano* **2018**, *12*, 11417–11425.
[116] Shi, X. L.; Zou, J.; Chen, Z. G. Advanced thermoelectric design: From materials and structures to devices. *Chem. Rev.* **2020**, *120*, 7399–7515.
[117] Yang, J.; Xi, L. L.; Qiu, W. J.; Wu, L. H.; Shi, X.; Chen, L. D.; Yang, J. H.; Zhang, W. Q.; Uher, C.; Singh, D. J. On the tuning of electrical and thermal transport in thermoelectrics: An integrated theory-experiment perspective. *Npj Comput. Mater.* **2016**, *2*, 15015.
[118] Kimberly, T. Q.; Wang, E. Y. C.; Navarro, G. D.; Qi, X.; Ciesielski, K. M.; Toberer, E. S.; Kauzlarich, S. M. Into the void: Single nanopore in colloidally synthesized Bi_2Te_3 nanoplates with ultralow lattice thermal conductivity. *Chem. Mater.* **2024**, *36*, 6618–6626.
[119] Li, J. H.; Shi, Q. W.; Röhr, J. A.; Wu, H.; Wu, B.; Guo, Y.; Zhang, Q. H.; Hou, C. Y.; Li, Y. G.; Wang, H. Z. Flexible 3D porous MoS_2/CNTs architectures with ZT of 0.17 at room temperature for wearable thermoelectric applications. *Adv. Funct. Mater.* **2020**, *30*, 2002508.
[120] He, P. L.; Wu, Y. Constructing of highly porous thermoelectric structures with improved thermoelectric performance. *Nano Res.* **2021**, *14*, 3608–3615.
[121] Lee, J. H.; Galli, G. A.; Grossman, J. C. Nanoporous Si as an efficient thermoelectric material. *Nano Lett.* **2008**, *8*, 3750–3754.
[122] Hu, Q. J.; Zhu, Z.; Zhang, Y. W.; Li, X. J.; Song, H. Z.; Zhang, Y. J. Remarkably high thermoelectric performance of $Cu_{2-x}Li_xSe$ bulks with nanopores. *J. Mater. Chem. A* **2018**, *6*, 23417–23424.
[123] Acharya, S.; Yu, B. K.; Hwang, J.; Kim, J.; Kim, W. High thermoelectric performance of ZnO by coherent phonon scattering and optimized charge transport. *Adv. Funct. Mater.* **2021**, *31*, 2105008.
[124] Zhao, L. W.; Qiu, W. B.; Sun, Y. X.; Chen, L. Q.; Deng, H.; Yang, L.; Shi, X. M.; Tang, J. Enhanced thermoelectric performance of $Bi_{0.3}Sb_{1.7}Te_3$ based alloys by dispersing TiC ceramic nanoparticles. *J. Alloys Compd.* **2021**, *863*, 158376.
[125] Cutler, M.; Leavy, J. F.; Fitzpatrick, R. L. Electronic transport in semimetallic cerium sulfide. *Phys. Rev.* **1964**, *133*, A1143–A1152.
[126] Zhu, Z.; Zhang, Y. W.; Song, H. Z.; Li, X. J. High thermoelectric performance and low thermal conductivity in $Cu_{2-x}Na_xSe$ bulk materials with micro-pores. *Appl. Phys. A* **2019**, *125*, 572.
[127] Wang, J. J.; Zhou, C. J.; Yu, Y.; Zhou, Y. X.; Lu, L.; Ge, B. Z.; Cheng, Y. D.; Jia, C. L.; Mazzarello, R.; Shi, Z. Q. et al. Enhancing thermoelectric performance of Sb_2Te_3 through swapped bilayer defects. *Nano Energy* **2021**, *79*, 105484.
[128] Tan, G. J.; Zhao, L. D.; Kanatzidis, M. G. Rationally designing high-performance bulk thermoelectric materials. *Chem. Rev.* **2016**, *116*, 12123–12149.
[129] Zhao, Y.; Li, Z. Y.; Wang, D. Y.; Zhang, X.; Ji, Z.; Niu, L. X.; Di, Y. Q.; Guan, Y.; Liu, L. Y.; Zou, Y. et al. High performance and colorful polymer thermoelectrics with imprinted porous film. *Adv. Mater.* **2024**, *36*, 2407692.
[130] Lee, Y.; Lo, S. H.; Chen, C. Q.; Sun, H.; Chung, D. Y.; Chasapis, T. C.; Uher, C.; Dravid, V. P.; Kanatzidis, M. G. Contrasting role of antimony and bismuth dopants on the thermoelectric performance of lead selenide. *Nat. Commun.* **2014**, *5*, 3640.
[131] Chen, Z. W.; Ge, B. H.; Li, W.; Lin, S. Q.; Shen, J. W.; Chang, Y. J.; Hanus, R.; Snyder, G. J.; Pei, Y. Z. Vacancy-induced dislocations within grains for high-performance PbSe thermoelectrics. *Nat. Commun.* **2017**, *8*, 13828.
[132] Wang, H.; LaLonde, A. D.; Pei, Y. Z.; Snyder, G. J. The criteria for beneficial disorder in thermoelectric solid solutions. *Adv. Funct. Mater.* **2013**, *23*, 1586–1596.
[133] Liu, H. T.; Sun, Q.; Zhong, Y.; Deng, Q.; Gan, L.; Lv, F. L.; Shi, X. L.; Chen, Z. G.; Ang, R. High-performance in n-type PbTe-based thermoelectric materials achieved by synergistically dynamic doping and energy filtering. *Nano Energy* **2022**, *91*, 106706.
[134] Jia, B. H.; Huang, Y.; Wang, Y.; Zhou, Y. S. Y.; Zhao, X. D.; Ning, S. T.; Xu, X.; Lin, P. J.; Chen, Z. Q.; Jiang, B. B. et al. Realizing high thermoelectric performance in non-nanostructured n-type PbTe. *Energy Environ. Sci.* **2022**, *15*, 1920–1929.
[135] Toprak, M. S.; Stiewe, C.; Platzek, D.; Williams, S.; Bertini, L.; Müller, E.; Gatti, C.; Zhang, Y.; Rowe, M.; Muhammed, M. The impact of nanostructuring on the thermal conductivity of thermoelectric $CoSb_3$. *Adv. Funct. Mater.* **2004**, *14*, 1189–1196.
[136] Liang, J.; Zhang, X. F.; Wan, C. L. From brittle to ductile: A scalable and tailorable all-inorganic semiconductor foil through a rolling process toward flexible thermoelectric modules. *ACS Appl. Mater. Interfaces* **2022**, *14*, 52017–52024.
[137] Liu, Y. J.; Wang, X. D.; Hou, S. H.; Wu, Z. X.; Wang, J.; Mao, J.; Zhang, Q.; Liu, Z. G.; Cao, F. Scalable-produced 3D elastic thermoelectric network for body heat harvesting. *Nat. Commun.* **2023**, *14*, 3058.
[138] Karthikeyan, V.; Surjadi, J. U.; Li, X. C.; Fan, R.; Theja, V. C. S.; Li, W. J.; Lu, Y.; Roy, V. A. L. Three dimensional architected thermoelectric devices with high toughness and power conversion efficiency. *Nat. Commun.* **2023**, *14*, 2069.
[139] Zhang, X.; Zhao, L. D. Thermoelectric materials: Energy conversion between heat and electricity. *J. Materiomics* **2015**, *1*, 92–105.
[140] He, R.; Schierning, G.; Nielsch, K. Thermoelectric devices: A review of devices, architectures, and contact optimization. *Adv. Mater. Technol.* **2018**, *3*, 1700256.
[141] Yan, Q. Y.; Kanatzidis, M. G. High-performance thermoelectrics and challenges for practical devices. *Nat. Mater.* **2022**, *21*, 503–513.
[142] Yang, L.; Chen, Z. G.; Han, G.; Hong, M.; Zou, Y. C.; Zou, J. High-performance thermoelectric Cu_2Se nanoplates through nanostructure engineering. *Nano Energy* **2015**, *16*, 367–374.
[143] Huang, S. Y.; Liu, Y.; Zhao, Y.; Ren, Z. F.; Guo, C. F. Flexible electronics: Stretchable electrodes and their future. *Adv. Funct. Mater.* **2019**, *29*, 1805924.
[144] Sun, T. T.; Zhou, B. Y.; Zheng, Q.; Wang, L. J.; Jiang, W.; Snyder, G. J. Stretchable fabric generates electric power from woven thermoelectric fibers. *Nat. Commun.* **2020**, *11*, 572.
[145] Chen, L. Z.; Lou, J.; Rong, X. H.; Liu, Z. Q.; Ding, Q. J.; Li, X.; Jiang, Y. F.; Ji, X. X.; Han, W. J. Super-stretching and high-performance ionic thermoelectric hydrogels based on carboxylated bacterial cellulose coordination for self-powered sensors. *Carbohydr. Polym.* **2023**, *321*, 121310.
[146] Kishore, R. A.; Nozariasbmarz, A.; Poudel, B.; Sanghadasa, M.; Priya, S. Ultra-high performance wearable thermoelectric coolers with less materials. *Nat. Commun.* **2019**, *10*, 1765.
[147] Russ, B.; Glaudell, A.; Urban, J. J.; Chabinyc, M. L.; Segalman, R. A. Organic thermoelectric materials for energy harvesting and temperature control. *Nat. Rev. Mater.* **2016**, *1*, 16050.
[148] Champier, D. Thermoelectric generators: A review of applications. *Energy Convers. Manage.* **2017**, *140*, 167–181.

[149] Simatupang, J. W.; Purnama, I. Study on various simple power tracking methods for thermoelectric generator. In *2019 International Conference on Sustainable Energy Engineering and Application* (*ICSEEA*), Tangerang, Indonesia, 2019, pp 79–84.
[150] Xu, H. W.; Zhang, Q.; Yi, L. B.; Huang, S. L.; Yang, H.; Li, Y. N.; Guo, Z.; Hu, H. Y.; Sun, P.; Tan, X. J. et al. High performance of Bi_2Te_3-based thermoelectric generator owing to pressure in fabrication process. *Appl. Energy* **2022**, *326*, 119959.
[151] Cui, G. P.; Feng, C. P.; Xu, S. C.; Sun, K. Y.; Ji, J. C.; Hou, L.; Lan, H. B.; Shang, H. J.; Ding, F. Z. 3D-printed Bi_2Te_3-based thermoelectric generators for energy harvesting and temperature response. *ACS Appl. Mater. Interfaces* **2024**, *16*, 35353–35360.
[152] Belovski, I.; Yovcheva, P.; Surchev, S.; Aleksandrov, A. Thermoelectric generator power prediction based on artificial neural network. In *2018 20th International Symposium on Electrical Apparatus and Technologies* (*SIELA*), Bourgas, Bulgaria, 2018, pp 1–4.
[153] Jung, S. J.; Shin, J.; Lim, S. S.; Kwon, B.; Baek, S. H.; Kim, S. K.; Park, H. H.; Kim, J. S. Porous organic filler for high efficiency of flexible thermoelectric generator. *Nano Energy* **2021**, *81*, 105604.
[154] Lv, H. C.; Liang, L. R.; Zhang, Y. C.; Deng, L.; Chen, Z. J.; Liu, Z. X.; Wang, H. F.; Chen, G. M. A flexible spring-shaped architecture with optimized thermal design for wearable thermoelectric energy harvesting. *Nano Energy* **2021**, *88*, 106260.
[155] Bertoldi, K.; Vitelli, V.; Christensen, J.; van Hecke, M. Flexible mechanical metamaterials. *Nat. Rev. Mater.* **2017**, *2*, 17066.
[156] Giulia, P. Thermoelectric materials: The power of pores. *Nat. Rev. Mater.* **2017**, *2*, 17006.
[157] Lee, M. H.; Yun, J. H.; Kim, G.; Lee, J. E.; Park, S. D.; Reith, H.; Schierning, G.; Nielsch, K.; Ko, W.; Li, A. P. et al. Synergetic enhancement of thermoelectric performance by selective charge anderson localization-delocalization transition in n-type Bi-doped PbTe/Ag_2Te nanocomposite. *ACS Nano* **2019**, *13*, 3806–3815.
[158] Roychowdhury, S.; Ghosh, T.; Arora, R.; Samanta, M.; Xie, L.; Singh, N. K.; Soni, A.; He, J. Q.; Waghmare, U. V.; Biswas, K. Enhanced atomic ordering leads to high thermoelectric performance in $AgSbTe_2$. *Science* **2021**, *371*, 722–727.
[159] Zhang, Y. X.; Huang, Q. Y.; Yan, X.; Wang, C. Y.; Yang, T. Y.; Wang, Z. Y.; Shi, Y. C.; Shan, Q.; Feng, J.; Ge, Z. H. Synergistically optimized electron and phonon transport in high-performance copper sulfides thermoelectric materials via one-pot modulation. *Nat. Commun.* **2024**, *15*, 2736.
[160] Jiang, Y. L.; Su, B.; Yu, J. C.; Han, Z. R.; Hu, H. H.; Zhuang, H. L.; Li, H. Z.; Dong, J. F.; Li, J. W.; Wang, C. et al. Exceptional figure of merit achieved in boron-dispersed GeTe-based thermoelectric composites. *Nat. Commun.* **2024**, *15*, 5915.
[161] Kim, J.; Bae, E. J.; Kang, Y. H.; Lee, C.; Cho, S. Y. Elastic thermoelectric sponge for pressure-induced enhancement of power generation. *Nano Energy* **2020**, *74*, 104824.
[162] Han, X.; Yang, X.; Zhang, K. A conformable and stretchable thermoelectric generator for efficient body heat harvesting. *ACS Appl. Electron. Mater.* **2024**, *6*, 8608–8616.
[163] Hu, Q. X.; Liu, W. D.; Zhang, L.; Sun, W.; Gao, H.; Shi, X. L.; Yang, Y. L.; Liu, Q. F.; Chen, Z. G. SWCNTs/Ag_2Se film with superior bending resistance and enhanced thermoelectric performance via *in situ* compositing. *Chem. Eng. J.* **2023**, *457*, 141024.
[164] Zhu, W. C.; Xu, A. Q.; Yang, W. L.; Xiong, B. Y.; Xie, C. J.; Li, Y.; Xu, L. M.; Shi, Y.; Lin, W. Optimal design of annular thermoelectric generator with twisted tape for performance enhancement. *Energy Convers. Manage.* **2022**, *270*, 116258.
[165] Zaia, E. W.; Gordon, M. P.; Yuan, P. Y.; Urban, J. J. Progress and perspective: Soft thermoelectric materials for wearable and internet-of-things applications. *Adv. Electron. Mater.* **2019**, *5*, 1800823.
[166] Chen, Y. N.; Zhao, Y.; Liang, Z. Q. Solution processed organic thermoelectrics: Towards flexible thermoelectric modules. *Energy Environ. Sci.* **2015**, *8*, 401–422.
[167] He, M. H.; Zhao, Y.; Wang, B.; Xi, Q.; Zhou, J.; Liang, Z. Q. 3D printing fabrication of amorphous thermoelectric materials with ultralow thermal conductivity. *Small* **2015**, *11*, 5889–5894.
[168] Li, H. B.; Zong, Y. D.; He, J.; Ding, Q. J.; Jiang, Y. F.; Li, X.; Han, W. J. Wood-inspired high strength and lightweight aerogel based on carbon nanotube and nanocellulose fiber for heat collection. *Carbohydr. Polym.* **2022**, *280*, 119036.
[169] Falanga, V.; Isseroff, R. R.; Soulika, A. M.; Romanelli, M.; Margolis, D.; Kapp, S.; Granick, M.; Harding, K. Chronic wounds. *Nat. Rev. Dis. Primers* **2022**, *8*, 50.
[170] Kamoun, E. A.; Kenawy, E. R. S.; Chen, X. A review on polymeric hydrogel membranes for wound dressing applications: PVA-based hydrogel dressings. *J. Adv. Res.* **2017**, *8*, 217–233.
[171] O'Brien, J. F.; Grace, P. A.; Perry, I. J.; Hannigan, A.; Clarke Moloney, M.; Burke, P. E. Randomized clinical trial and economic analysis of four-layer compression bandaging for venous ulcers. *Br. J. Surg.* **2003**, *90*, 794–798.
[172] Zhao, M.; Song, B.; Pu, J.; Wada, T.; Reid, B.; Tai, G. P.; Wang, F.; Guo, A. H.; Walczysko, P.; Gu, Y. et al. Electrical signals control wound healing through phosphatidylinositol-3-OH kinase-γ and PTEN. *Nature* **2006**, *442*, 457–460.
[173] Willenborg, S.; Eming, S. A. Cellular networks in wound healing. *Science* **2018**, *362*, 891, 892.
[174] Vanhaesebroeck, B. Charging the batteries to heal wounds through PI3K. *Nat. Chem. Biol.* **2006**, *2*, 453–455.
[175] Logothetis, I.; Gkoutzeli, D.; Kagkas, D.; Vassiliadis, S.; Siores, E.; Pirogova, E. Thermoelectric heat patch for clinical and self-management: Melanoma excision wound care. *Ann. Biomed. Eng.* **2019**, *47*, 537–548.
[176] Gao, Y. F.; Zhu, S. J.; Gao, J.; Miao, L.; Xu, F.; Sun, L. X. Wearable thermoelectric cooler encapsulated with low thermal conductivity filler and honeycomb structure for high cooling effect. *Mater. Today Phys.* **2024**, *46*, 101491.
[177] Gao, X. Z.; Gao, F. L.; Liu, J.; Li, Y. J.; Wan, P. B.; Yu, Z. Z.; Li, X. F. Self-powered resilient porous sensors with thermoelectric poly(3,4-ethylenedioxythiophene): Poly(styrenesulfonate) and carbon nanotubes for sensitive temperature and pressure dual-mode sensing. *ACS Appl. Mater. Interfaces* **2022**, *14*, 43783–43791.
[178] Yang, L.; Chen, X.; Dutta, A.; Zhang, H.; Wang, Z. H.; Xin, M. Y.; Du, S. J.; Xu, G. Z.; Cheng, H. Y. Thermoelectric porous laser-induced graphene-based strain–temperature decoupling and self-powered sensing. *Nat. Commun.* **2025**, *16*, 792.
[179] Deng, Q.; Shi, X. L.; Li, M.; Tan, X. B.; Li, R. H.; Wang, C.; Chen, Y.; Dong, H. L.; Ang, R.; Chen, Z. G. Lattice defect engineering advances n-type PbSe thermoelectrics. *Nat. Commun.* **2025**, *16*, 656.
[180] Deng, T. T.; Gao, Z. Q.; Li, Z.; Qiu, P. F.; Li, Z.; Yuan, X. J.; Ming, C.; Wei, T. R.; Chen, L. D.; Shi, X. Room-temperature exceptional plasticity in defective Bi_2Te_3-based bulk thermoelectric crystals. *Science* **2024**, *386*, 1112–1117.
[181] Siddique, S.; Abbas, G.; Yaqoob, M. M.; Zhao, J.; Chen, R. H.; Larsson, J. A.; Cao, Y. D.; Chen, Y. X.; Zheng, Z. H.; Zhang, D. P. et al. Optimization of thermoelectric performance in p-type SnSe crystals through localized lattice distortions and band convergence. *Adv. Sci.* **2024**, *12*, 2411594.